a separation distance of 36 cm. The gels were scanned using a laser scanner (Typhoon Trio, GE Healthcare Biosciences) at the appropriate wavelength for Cy3 or Cy5. For all protein spots, the Cy5 intensity was normalized with the Cy3 intensity in the same gel using the Progenesis SameSpots software version 3 (Nonlinear Dynamics, Newcastle, UK), so that gel-to-gel variations were eliminated (Fig. 1B). All samples were examined in triplicate gels and the mean normalized intensity value was used for the analysis.

2.6. *Data analysis*

The spot intensity data were subjected to scatter plot, hierarchical clustering analysis and Wilcoxson test using the Expressionist software (GeneData, Basel, Switzerland).

2.7. *Mass spectrometric protein identification*

The proteins corresponding to the spots of interest were identified by mass spectrometry [20]. In brief, 100 μg of protein samples were labeled with Cy5, and separated by 2D-PAGE. Then proteins were recovered and digested with modified trypsin (Promega, Madison, WI). The trypsin digests were subjected to liquid chromatography coupled with tandem mass spectrometry equipped with a nanoelectrospray ion source (Finnigan LTQ linear ion trap mass spectrometer, Thermo Electron Co., San Jose, CA). The Mascot software (version 2.2; Matrix Science, London, UK) was used to search for the mass of the peptide ion peaks against the SWISS-PROT database (Homo sapiens, 471472 sequences in Sprot_57.5.fasta file). Proteins with a Mascot score of 34 or more were considered as positively identified. When multiple proteins were identified in a single spot, the proteins with the highest number of peptides were considered as those corresponding to the spot (Supplementary Table 3).

2.8. *Western blotting*

Protein samples were separated by sodium dodecyl sulfate (SDS)-PAGE and subsequently blotted on a nitrocellulose membrane. Western blotting was performed using antibodies to CapG (1:500; Proteintech Group, Inc, Chicago, IL) and actin (1:250; Sigma, Saint Louis, MO), and horseradish peroxidase-conjugated secondary antibodies (1:1,000; GE Healthcare Biosciences). The immunocomplex was detected by the enhanced chemiluminescence system (ECL Plus; GE Healthcare Biosciences) and LAS-3000 (Fuji Photo Film , Tokyo, Japan).

2.9. *Immunohistochemistry*

Immunohistochemical staining for CapG was performed on formalin-fixed and paraffin-embedded tissue sections using a polymer-based method (Envision Dual Ling System-HRP, Dako, DK-2600 , Glostrup, Denmark). The sections were deparaffinized, dehydrated and treated with 10 ml/l H_2O_2 in methanol for 30 min to remove endogenous peroxidase activity. For antigen retrieval, the sections were autoclaved in 10 mM citrate buffer (pH 6.0) at 121 °C for 10 min. The antibody to CapG (Proteintech Group, Chicago, IL) was used at a dilution of 1:500. The sections were visualized using 3,30-diaminobenzidine tetrahydrochloride as a chromogen. Finally, the sections were couterstained with hematoxylin. Staining was assessed by two independent observers in a blinded fashion for clinical data (H.O. and N.M.). Possible discrepancies between the observers were solved by discussion and re-examination.

2.10. *Statistical analysis*

Associations between the results of immunohistochemistry and clinicopathological factors were assessed by the $\chi 2$ test. Cumulative survival rates and survival curves were calculated by the Kaplan–Meier method [21]. The log-rank test was performed for the comparison of survival curves. Cox's proportional hazard model was performed to estimate the hazard ratio (HR) and 95% confidence interval (CI) of outcome. Multivariate analyses were performed using risk factors for outcome. Risk factors with p value less than 0.05 were considered to be significant. Statistical analyses were performed using the SPSS 11.0 statistical package (SPSS, Chicago, IL).

3. Results

The generated protein expression profiles of the cholangiocarcinoma cell lines and tumors examined consisted of 3571 protein spots (Supplementary Table 2). The spot numbers in Supplementary Table 2 were defined using Progenesis SameSpot, and commonly used for all gels. We monitored the system reproducibility by running Sample 3 (Table 1) twice. The scatter plot showed that the intensity value of 91.2% of protein spots was scattered within a 2-fold value difference, and that the correlation coefficient of the paired intensity for all protein spots was 0.8167, demonstrating the high reproducibility of our profiling method using 2D-DIGE (Fig. 1C). We compared the profiles of the groups with different response to GEM treatment. The result of comparative studies is summarized as a heat-map in Fig. 2. Among the 3571 protein spots detected in total, we identified 17 spots whose intensity was different (more than two fold difference, Wilcoxson $p<0.05$) between the sensitive and resistant cell line group, and 38 spots whose intensity was different between the sensitive and resistant xenograft group. We also found 117 protein spots whose intensity was different between the effective and non-effective group of cases. Total number of protein spots identified was 172 as certain identical protein spots repeatedly showed the intensity differences. We identified 156 distinct gene products corresponding to all these 172 protein spots by mass spectrometry (Supplementary Table 3). The results of the expression study and protein identification are demonstrated as a heatmap in Fig. 2, and the localization of the identified protein spots and the results of protein identification are exhibited in our database (Genome Medicine Database of Japan Proteomics, GeMDBJ Proteomics, https://gemdbj.nibio.go.jp/dgdb/DigeTop.do) and Supplementary Table 3. Hierarchical clustering showed that protein samples were grouped according to the response to GEM treatment on the basis of the intensity of 172 protein spots. Three proteins, cytokeratin

Fig. 2 – Results of protein expression study by 2D-DIGE and protein identification by mass spectrometry. (A) cell lines, (B) xenografts, and (C) primary tumors. The protein samples were grouped according to the response to GEM treatment based on the intensity of 17, 38, and 117 protein spots in (A), (B) and (C), respectively. The numbers of the sample and protein spots correspond to those in Table 1 and Supplementary Table 3.

9 (KRT9), cytokeratin 10 (KRT10) and macrophage capping protein (CapG), were commonly detected as proteins with different expression between the groups compared using cell lines, xenografts, and surgically resected tumors (Fig. 2). Although macrophage-capping protein could be detected as the difference proteins at three positions, namely spots 255, 447 and 2113 (Fig. 3A), the expression of these three species was different among samples. Specifically, cultured cancer cells expressed only spot 447 species, while the xenografts of these cells showed expression of spot 255 and 2113 isoforms. In contrast, the cancer tissues in surgical specimens showed expression of spot 255 only. These observations were summarized in Fig. 3B.

We further validated the relationship of the expression of these three proteins with response to GEM treatment by western blotting. As laser microdissection did not yield adequate amounts of protein from the primary tumors, we only examined cell lines and xenografts. Western blotting showed that the expression of CapG was inversely correlated with response to GEM treatment. This finding was correlated significantly with the corresponding 2D-DIGE results (Fig. 4A) in both the cell line (correlation coefficient: 0.509 in spot No. 447) and the xenograft (correlation coefficient: 0.503 in spot No.255, 0.652 in spot No. 2213) sample subset. We found that the Western blotting data for KRT9 and KRT10 did not correlate with 2D-DIGE data in either the cell line or the xenograft samples (data not shown).

We performed immunohistochemistry to evaluate CapG expression in cell lines, xenografts and surgically resected primary tumors. The intensity of CapG staining was defined as follows: 2+, strong cytoplasmic and/or nuclear staining in ≥30% cancer cells; 1+, faint or moderate cytoplasmic staining and no nuclear staining in ≥50% cancer cells, if 2+ cancer cells <30%; 0, faint or moderate cytoplasmic staining and no nuclear staining in <50% cancer cells, if 2+ cancer

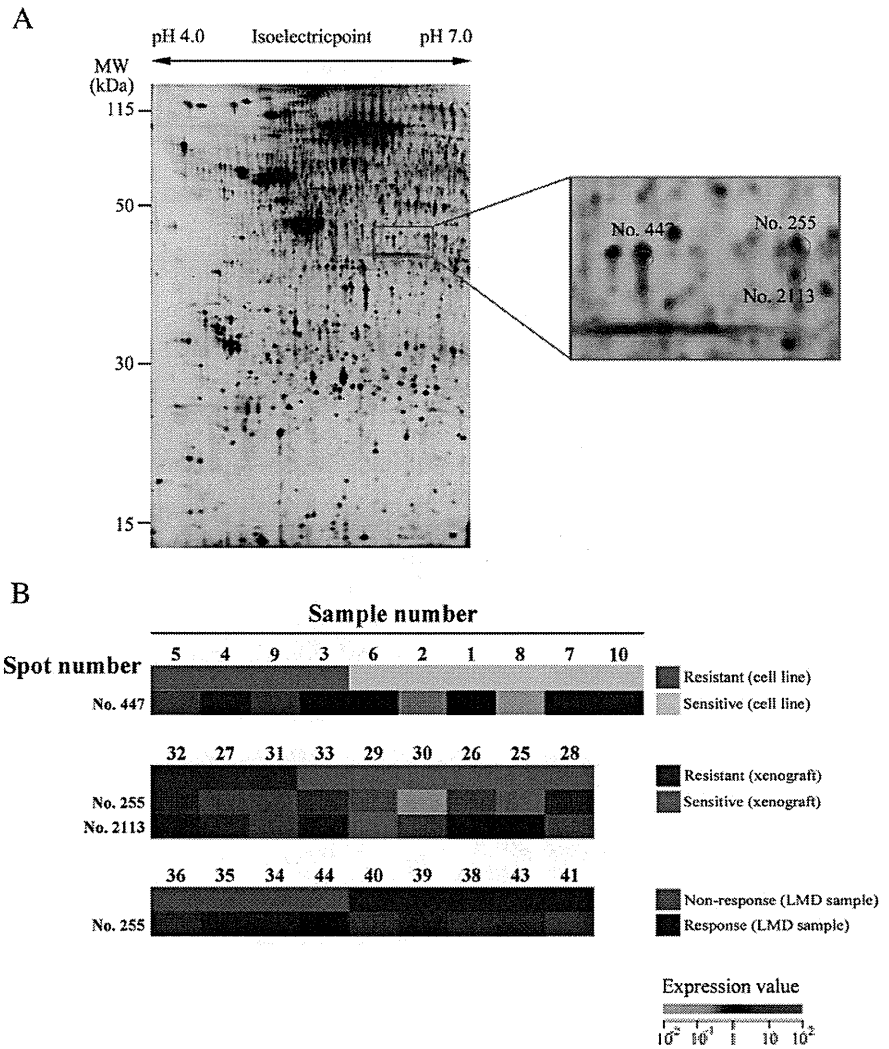

Fig. 3 – Intensity and localization of protein spots for CapG. A. The localization of CapG isoforms on the 2D image. The number of spots corresponds to those in Fig. 2. The 2D image was created by the internal control sample. B. Intensity of protein spots for CapG was exhibited by heat-maps. The protein spots with statistically (Wilcoxson p value less than 0.05) and significantly (more than 2 fold) different intensity between the groups are demonstrated with the spot number. Note that the protein spots for CapG with different intensity were unique to the sample sets.

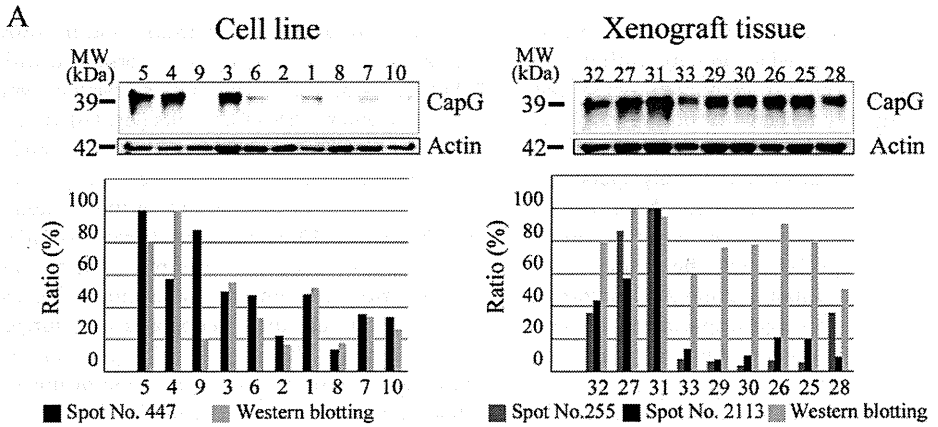

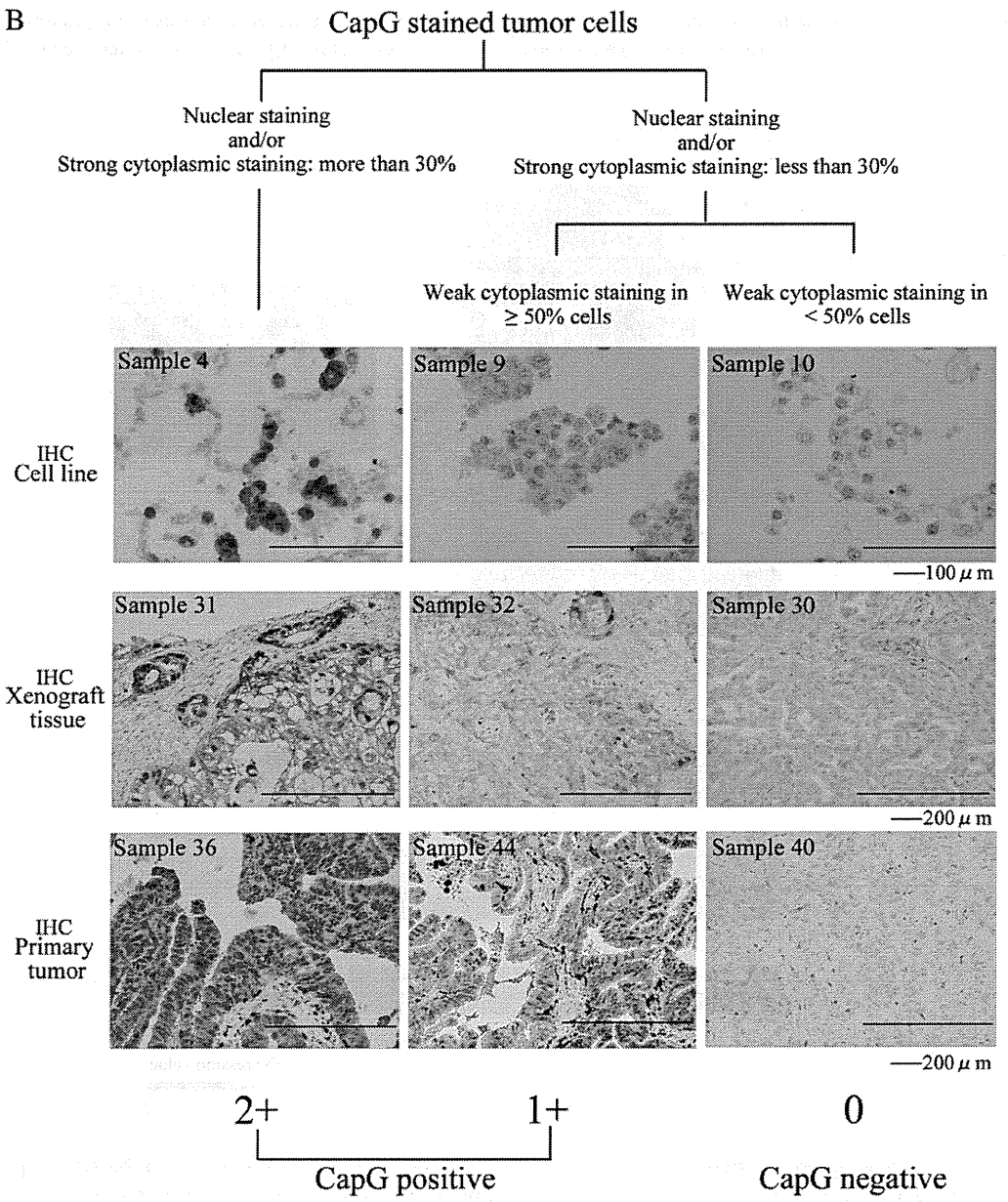

Table 2 – Immunohistochemistry results based on the criteria shown in .

Sample number [a]	Cell line [b,e]	GEM	CapG [d]			CapG IHC [d]
		Sensitive or resistant [c,f]	No staining (%)	Weak staining (%)	Strong staining (%)	
Cell lines						
5	NCC-CC1	Resistant	0	10	90	2+ (positive)
4	OZ	Resistant	70	0	30	2+ (positive)
9	NCC-BD2	Resistant	50	50	0	1+ (positive)
3	TKKK	Resistant	30	30	40	2+ (positive)
6	NCC-BD1	Sensitive	80	0	20	0 (negative)
2	Hucct1	Sensitive	80	15	5	0 (negative)
1	TGBC24TKB	Sensitive	20	30	50	2+ (positive)
8	NCC-CC4-1	Sensitive	100	0	0	0 (negative)
7	NCC-CC3-2	Sensitive	60	40	0	0 (negative)
10	NCC-CC3-1	Sensitive	80	20	0	0 (negative)
Xenografts						
32	NCC-CC1	Resistant	0	70	30	2+ (positive)
27	OZ	Resistant	0	50	50	2+ (positive)
31	TKKK	Resistant	0	10	90	2+ (positive)
33	NCC-CC4-1	Sensitive	80	5	15	0 (negative)
29	NCC-CC3-1	Sensitive	100	0	0	0 (negative)
30	NCC-CC3-2	Sensitive	100	0	0	0 (negative)
26	TGBC24TKB	Sensitive	70	20	10	0 (negative)
25	Hucct1	Sensitive	60	40	0	0 (negative)
28	NCC-BD1	Sensitive	90	10	0	0 (negative)

Primary tumor tissues with recurrence undergoing gemcitabine therapy after surgery

Sample number [a]	Duration of SD [g]	CapG [d]			CapG IHC [d]
		No staining (%)	Weak staining (%)	Strong staining (%)	
34	LT6	0	60	40	2+ (positive)
35	LT6	0	20	80	2+ (positive)
36	LT6	0	30	70	2+ (positive)
44	LT6	0	90	10	1+ (positive)
38	MT6	20	60	20	1+ (positive)
43	MT6	100	0	0	0 (negative)
41	MT6	100	0	0	0 (negative)
39	MT6	70	30	0	0 (negative)
40	MT6	100	0	0	0 (negative)

[a] Sample numbers correspond to those in GeMDBJ Proteomics (https://gemdbj.nibio.go.jp/dgdb/DigeTop.do).
[b] The characters of cell lines were described in our previous paper (16).
[c] *In vitro* assay for determining the sensitivity for the treatment with gemcitabine was detailed in our previous paper (16).
[d] CapG, macrophage-capping protein. IHC, immunohistochemistry. The diagram of CapG classification is described in Fig. 4.
[e] These cell lines provided the material used for transplantation.
[f] Determining the sensitivity was based on the drug sensitivity of the original cell lines.
[g] The duration of the period in which the disease was stable (SD) after treatment with gemcitabine; LT6, less than 6 months; MT6, more than 6 months.

cells <30%. Samples with an immunohistochemical score of 1+ or 2+ were defined as positive and the others as negative (Fig. 4B). Under these criteria, we divided the cases into the CapG positive and negative groups. As shown in Table 2, all four "resistant" cell lines (100%), and one of six "sensitive" cell lines (17%) were CapG positive. All three resistant xenografts (100%) were CapG positive, and all six sensitive xenografts (100%) were CapG negative. All four samples from the non-effective group (100%) and one of five samples from the effective group (20%) were CapG positive. These immunohistochemistry

Fig. 4 – (A) Western blotting. The sample numbers correspond to those in Table 1. Upper panel; Western blotting image. Lower panel; the corresponding quantified data of 2D-DIGE and Western blotting. The ratio of standardized intensity of protein spots for CapG in 2D-DIGE and the intensity of protein bands for CapG in Western blotting are demonstrated. (B) The diagram demonstrates the scoring system used for CapG staining. CapG staining was scored as 0, 1+, or 2+. A score of 1+ or 2+ was defined as positive, and the score of 0 was defined as negative. Typical images for CapG positive and negative staining are shown.

results confirmed the correlation between CapG expression and response to GEM treatment observed in the generated protein expression profiles.

Overexpression of CapG has been reported in various types of malignancies [22–27]. In addition, *in vitro* experiments using breast and pancreatic cancer cell lines demonstrated that CapG plays a key role in metastasis and invasion [22,24,28]. We used immunohistochemistry to examine CapG expression in an additional set of 196 cholangiocarcinoma cases that did not receive GEM treatment alone and that were not included in the proteomic study. In 123 EHCC cases, but not 73 IHCC cases, CapG-positive and CapG-negative tumors had significantly different macroscopic type, histological type, lymphatic invasion status and surgical resection procedure in univariate analysis (Supplementary Table 1). Because CapG expression was correlated with established prognostic parameters, such as lymphatic invasion [29,30], in the EHCC cases (Supplemental Table 1), we further investigated the prognostic value of CapG expression. The Kaplan–Meier survival curve showed that patients with CapG-positive cholangiocarcinoma had significantly worse prognosis than those with CapG-negative one in terms of overall survival rate (EHCC, $p=0.047$; IHCC, $p=0.021$) (Fig. 5). Univariate and multivariate analyses revealed that CapG was an independent prognostic factor for overall survival (EHCC: HR, 1.89; 95% CI, 1.11–3.20; $p=0.018$, IHCC: HR, 2.26; 95% CI, 1.23–4.14; $p=0.008$), along with other established clinicopathological parameters such as the macroscopic type, degree of differentiation, venous involvement, and lymph node metastasis (Table 3).

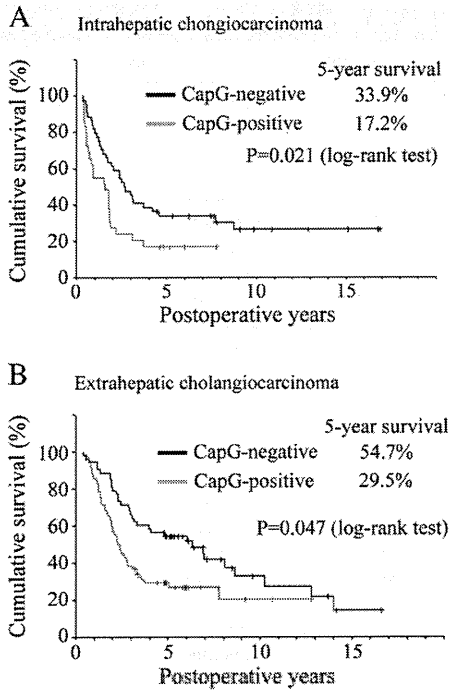

Fig. 5 – Survival curves stratified by CapG expression in (A) intrahepatic and (B) extrahepatic cholangiocarcinoma (Kaplan–Meier method). The outcome for the CapG-positive cases was significantly worse than that for the CapG-negative cases in both intrahepatic ($P=0.021$) and extrahepatic cholangiocarcinoma ($P=0.047$) (by log-rank test).

4. Discussions

GEM has been used in the treatment of various types of malignancies [31–34]. However, since only a limited number of patients has benefited from GEM treatment, novel biomarkers are required to predict the response to treatment and hence to optimize the therapeutic strategy.

Previous global studies and studies on individual genes for GEM resistance revealed that the expression levels of human equilibrative nucleoside transporter-1 (hENT1), deoxycytidine kinase (dCK), ribonucleotide reductase M1 and M2 (RRM1 and RRM2) [35], and heat shock protein 27 (Hsp27) in pancreatic cancer cells [36], correlated with gemcitabine-resistance, and that the expression levels of ribonucleotide reductase M1 [37], activation of checkpoint kinases, Chk2 and Chk1, extracellular signal-regulated kinase (ERK)1/2 [38], eukaryotic initiation factor 4E [39], micro-RNAs [40] and melanoma antigen family H 1 (MAGEH1) [16] were also associated with gemcitabine resistance in cholangiocarcinoma cells. In contrast, although the use of a proteomic approach has been proven to be effective for biomarker development [41], only two proteomic studies have examined the molecular backgrounds of the different response to GEM treatment [36,42], and there is no report on CapG expression in relation to GEM treatment in cholangiocarcinoma.

CapG controls actin-based motility by capping the bared ends of actin filaments [43]. CapG overexpression has been previously detected in a range of malignancies [23–26] probably having a role in the control of cell mobility, invasiveness, and metastasis in cancer cells [28,44]. However, the association between CapG expression and response to GEM treatment in cholangiocarcinoma has not been examined to date.

We found that CapG expression was significantly associated with histologic evidence of lymphatic invasion status, one of the dominant prognostic factors in EHCC [29]. We subsequently examined the relation of CapG expression with overall survival and found that patients with CapG-positive cholangiocarcinoma had significantly shorter survival than those with CapG-negative tumors irrespective of tumor location. Multivariate analysis revealed that CapG expression was an independent prognostic factor for survival of IHCC and EHCC patients. Although we did not identify the clinicopathological prognostic parameters associated with CapG expression in IHCC, our results show that CapG expression is a biomarker that has prognostic value and is possibly predictive of the response to GEM treatment in cholangiocarcinoma.

The three experiment model types used in this study have unique advantages for cancer research. Cell line and xenograft models provide preclinical experimental platforms, where the effects of drug treatment on cell phenotypes and target molecules can be repeatedly and easily assessed. Cell line models, albeit artificial, are easy to use and suitable for pharmacokinetics and pharmacodynamics studies, while xenograft models simulate human disease more accurately

Table 3 – Overall survival.

Survival		Adjusted HR	95% CI	p value
Total (73 IHCC cases)				
Macroscopic type	Non-mass forming	1.00		
	Mass forming	4.29	1.78, 10.36	0.001
Differentiation of adenocarcinoma	Well	1.00		
	Mod	1.05	0.46, 2.41	0.914
	Por	5.84	1.30, 26.24	0.021
Venous invasion	Negative	1.00		
	Positive	8.30	2.10, 32.81	0.003
CapG	Negative	1.00		
	Positive	2.68	1.52, 4.72	0.001
Total (123 EHCC cases)				
Differentiation of adenocarcinoma	Well	1.00		
	Mod	1.45	0.86, 2.44	0.165
	Por	4.34	2.10, 8.98	< 0.001
Venous invasion	Negative	1.00		
	Positive	4.20	1.54, 11.41	0.005
UICC pN	pN0	1.00		
	pN1	2.10	1.29, 3.40	0.003
Surgical resection procedure	PD	1.00		
	EHBR	1.13	0.40, 3.23	0.817
	HR+EHBR	1.94	1.10, 3.42	0.022
	HR	5.97	1.26, 28.29	0.024
	HPD	2.45	0.96, 6.25	0.061
CapG	Negative	1.00		
	Positive	1.74	1.06, 2.88	0.030

Abbreviation: HR, hazard ratio; CI, confidence interval; Well, well differentiated adenocarcinoma; Mod, moderately differentiated adenocarcinoma; Por, poorly differentiated adenocarcinoma; PD, pancreatoduodenectomy; EHBR, extrahepatic bile duct resection; HR, hepatic resection; HPD, hepatopancreatoduodenectomy.

[45]. The study of expression using primary tumor tissues provides data on the actual molecular events occurring in patients, however, experiments requiring living cells cannot be done using clinical materials. We identified CapG as a protein predictive of the response to gemcitabin treatment using all the aforementioned model types. Unique CapG isoforms were observed in each of the three experimental systems (Fig. 3B), and the functional difference of these three isoforms remains to be elucidated. The molecular backgrounds generating these isoforms are presently not clear. Each isoform may have its own functions, and certain common properties may associate with the malignant potentials examined in this study. In any case, as the association of the total amount of CapG with poor prognosis was proven in a large sample set (196 cases), further consideration of the clinical utility of CapG expression in personalized medicine may be warranted. The patients with CapG-positive tumor may have worse prognosis and exhibit resistance to GEM treatment. More intense treatments using presently available therapies, or development of novel drugs for such patients should be considered.

As CapG expression was correlated with both the sensitivity to GEM treatments and poor prognosis, it may be involved in the overall molecular mechanisms underlying the malignant potentials of cholangiocarcinoma cells. Previous studies suggested that CapG contributed to the cell motility in pancreatic cancer cells [24]. Thus, it is worthy challenging to explore the possibility of CapG as a therapeutic target.

5. Conclusions

We studied the proteomic profile of cholangiocarcinoma using three well-characterized sources of material. We identified CapG expression as a novel biomarker predictive of response to GEM treatment and as a prognostic indicator in cholangiocarcinoma. Although the number of cases in this study was still limited and the further validation studies should be needed before clinical applications, the inclusion of CapG expression in the diagnostic arsenal may lead the novel strategies for cholangiocarcinoma management. The cholangiocarcinoma patients who have CapG-positive primary tumor may need more intense therapy, other than that with GEM. The applications of CapG may be also worth challenged in the cholangiocarcinoma.

Supplementary materials related to this article can be found online at doi:10.1016/j.jprot.2011.11.030.

Acknowledgements

The excellent technical support of Ms. Yukiko Kobori and Ms. Yukako Tsunehiro in electrophoresis, and Ms. Hiroko Shimizu in cell culture and is greatly appreciated. The authors thank Setsuo Hirohashi, M.D., Ph.D. for discussion. This work was supported by the Ministry of Health, Labor and Welfare, and

by the Program for Promotion of Fundamental Studies in Health Sciences of the Organization for Pharmaceutical Safety and Research of Japan and grants from the Foundation for Promotion of Cancer Research. N.M. is a Research Resident Fellowship awardee from the Foundation for Promotion of Cancer Research in Japan.

REFERENCES

[1] Yonemoto N, Furuse J, Okusaka T, Yamao K, Funakoshi A, Ohkawa S, et al. A multi-center retrospective analysis of survival benefits of chemotherapy for unresectable biliary tract cancer. Jpn J Clin Oncol 2007;37:843–51.
[2] Briggs CD, Neal CP, Mann CD, Steward WP, Manson MM, Berry DP. Prognostic molecular markers in cholangiocarcinoma: a systematic review. Eur J Cancer 2009;45:33–47.
[3] Khan SA, Thomas HC, Davidson BR, Taylor-Robinson SD. Cholangiocarcinoma. Lancet 2005;366:1303–14.
[4] Bonney GK, Craven RA, Prasad R, Melcher AF, Selby PJ, Banks RE. Circulating markers of biliary malignancy: opportunities in proteomics? Lancet Oncol 2008;9:149–58.
[5] Washburn WK, Lewis WD, Jenkins RL. Aggressive surgical resection for cholangiocarcinoma. Arch Surg 1995;130:270–6.
[6] Kosuge T, Yamamoto J, Shimada K, Yamasaki S, Makuuchi M. Improved surgical results for hilar cholangiocarcinoma with procedures including major hepatic resection. Ann Surg 1999;230:663–71.
[7] Jang JY, Kim SW, Park DJ, Ahn YJ, Yoon YS, Choi MG, et al. Actual long-term outcome of extrahepatic bile duct cancer after surgical resection. Ann Surg 2005;241:77–84.
[8] Sakamoto Y, Kosuge T, Shimada K, Sano T, Ojima H, Yamamoto J, et al. Prognostic factors of surgical resection in middle and distal bile duct cancer: an analysis of 55 patients concerning the significance of ductal and radial margins. Surgery 2005;137:396–402.
[9] Orimo T, Ojima H, Hiraoka N, Saito S, Kosuge T, Kakisaka T, et al. Proteomic profiling reveals the prognostic value of adenomatous polyposis coli-end-binding protein 1 in hepatocellular carcinoma. Hepatology 2008;48:1851–63.
[10] Xu Y, Zhang SZ, Huang CH, Liu XY, Zhong ZH, Hou WL, et al. Keratin 17 identified by proteomic analysis may be involved in tumor angiogenesis. BMB Rep 2009;42:344–9.
[11] Kawase H, Fujii K, Miyamoto M, Kubota KC, Hirano S, Kondo S, et al. Differential LC-MS-based proteomics of surgical human cholangiocarcinoma tissues. J Proteome Res 2009;8: 4092–103.
[12] Wang X, Dai S, Zhang Z, Liu L, Wang J, Xiao X, et al. Characterization of apolipoprotein A-I as a potential biomarker for cholangiocarcinoma. Eur J Cancer Care (Engl) 2009;18:625–35.
[13] Matsubara J, Ono M, Negishi A, Ueno H, Okusaka T, Furuse J, et al. Identification of a predictive biomarker for hematologic toxicities of gemcitabine. J Clin Oncol 2009;27:2261–8.
[14] Takano S, Togawa A, Yoshitomi H, Shida T, Kimura F, Shimizu H, et al. Annexin II overexpression predicts rapid recurrence after surgery in pancreatic cancer patients undergoing gemcitabine-adjuvant chemotherapy. Ann Surg Oncol 2008;15:3157–68.
[15] Kondo T, Hirohashi S. Application of highly sensitive fluorescent dyes (CyDye DIGE Fluor saturation dyes) to laser microdissection and two-dimensional difference gel electrophoresis (2D-DIGE) for cancer proteomics. Nat Protoc 2006;1:2940–56.
[16] Ojima H, Yoshikawa D, Ino Y, Shimizu H, Miyamoto M, Kokubu A, et al. Establishment of six new human biliary tract carcinoma cell lines and identification of MAGEH1 as a candidate biomarker for predicting the efficacy of gemcitabine treatment. Cancer Sci 2009;101:882–8.
[17] Eisenhauer EA, Therasse P, Bogaerts J, Schwartz LH, Sargent D, Ford R, et al. New response evaluation criteria in solid tumours: revised RECIST guideline (version 1.1). Eur J Cancer 2009;45:228–47.
[18] Sobin LH, Wittekind C. International Union against Cancer (UICC) TNM Classification of Malignant Tumours. 6th ed. John Wiley & Sons; 2002.
[19] Kondo T, Seike M, Mori Y, Fujii K, Yamada T, Hirohashi S. Application of sensitive fluorescent dyes in linkage of laser microdissection and two-dimensional gel electrophoresis as a cancer proteomic study tool. Proteomics 2003;3:1758–66.
[20] Hatakeyama H, Kondo T, Fujii K, Nakanishi Y, Kato H, Fukuda S, et al. Protein clusters associated with carcinogenesis, histological differentiation and nodal metastasis in esophageal cancer. Proteomics 2006;6:6300–16.
[21] Kaplan EL, Meier P. Nonparametric-estimation from incomplete observations. J Am Stat Assoc 1958;53:457–81.
[22] Xu SG, Yan PJ, Shao ZM. Differential proteomic analysis of a highly metastatic variant of human breast cancer cells using two-dimensional differential gel electrophoresis. J Cancer Res Clin Oncol 2010;136:1545–56.
[23] Dahl E, Sadr-Nabavi A, Klopocki E, Betz B, Grube S, Kreutzfeld R, et al. Systematic identification and molecular characterization of genes differentially expressed in breast and ovarian cancer. J Pathol 2005;205:21–8.
[24] Thompson CC, Ashcroft FJ, Patel S, Saraga G, Vimalachandran D, Prime W, et al. Pancreatic cancer cells overexpress gelsolin family-capping proteins, which contribute to their cell motility. Gut 2007;56:95–106.
[25] Lal A, Lash AE, Altschul SF, Velculescu V, Zhang L, McLendon RE, et al. A public database for gene expression in human cancers. Cancer Res 1999;59:5403–7.
[26] Van Ginkel PR, Gee RL, Walker TM, Hu DN, Heizmann CW, Polans AS. The identification and differential expression of calcium-binding proteins associated with ocular melanoma. Biochim Biophys Acta 1998;1448:290–7.
[27] Nomura H, Uzawa K, Ishigami T, Kouzu Y, Koike H, Ogawara K, et al. Clinical significance of gelsolin-like actin-capping protein expression in oral carcinogenesis: an immunohistochemical study of premalignant and malignant lesions of the oral cavity. BMC Cancer 2008;8:1–8.
[28] Renz M, Betz B, Niederacher D, Bender HG, Langowski J. Invasive breast cancer cells exhibit increased mobility of the actin-binding protein CapG. Int J Cancer 2008;122:1476–82.
[29] Zerbi A, Balzano G, Leone BE, Angeli E, Veronesi P, Di Carlo V. Clinical presentation, diagnosis and survival of resected distal bile duct cancer. Dig Surg 1998;15:410–6.
[30] Shirabe K, Mano Y, Taketomi A, Soejima Y, Uchiyama H, Aishima S, et al. Clinicopathological prognostic factors after hepatectomy for patients with mass-forming type intrahepatic cholangiocarcinoma: relevance of the lymphatic invasion index. Ann Surg Oncol 2010;17:1816–22.
[31] Abbruzzese JL. New applications of gemcitabine and future directions in the management of pancreatic cancer. Cancer 2002;95:941–5.
[32] Lorusso D, Ferrandina G, Fruscella E, Marini L, Adamo V, Scambia G. Gemcitabine in epithelial ovarian cancer treatment: current role and future perspectives. Int J Gynecol Cancer 2005;15:1002–13.
[33] Moore MJ, Tannock IF, Ernst DS, Huan S, Murray N. Gemcitabine: a promising new agent in the treatment of advanced urothelial cancer. J Clin Oncol 1997;15:3441–5.
[34] Amadori D, Cecconetto L. Gemcitabine and taxanes in metastatic breast cancer. Ann Oncol 2006;17(Suppl. 5):v173–6.
[35] Nakano Y, Tanno S, Koizumi K, Nishikawa T, Nakamura K, Minoguchi M, et al. Gemcitabine chemoresistance and molecular markers associated with gemcitabine transport

and metabolism in human pancreatic cancer cells. Br J Cancer 2007;96:457–63.
[36] Mori-Iwamoto S, Kuramitsu Y, Ryozawa S, Mikuria K, Fujimoto M, Maehara S, et al. Proteomics finding heat shock protein 27 as a biomarker for resistance of pancreatic cancer cells to gemcitabine. Int J Oncol 2007;31:1345–50.
[37] Ohtaka K, Kohya N, Sato K, Kitajima Y, Ide T, Mitsuno M, et al. Ribonucleotide reductase subunit M1 is a possible chemoresistance marker to gemcitabine in biliary tract carcinoma. Oncol Rep 2008;20:279–86.
[38] Matsumoto K, Nagahara T, Okano J, Murawaki Y. The growth inhibition of hepatocellular and cholangiocellular carcinoma cells by gemcitabine and the roles of extracellular signal-regulated and checkpoint kinases. Oncol Rep 2008;20: 863–72.
[39] Wehbe H, Henson R, Lang M, Meng F, Patel T. Pifithrin-alpha enhances chemosensitivity by a p38 mitogen-activated protein kinase-dependent modulation of the eukaryotic initiation factor 4E in malignant cholangiocytes. J Pharmacol Exp Ther 2006;319:1153–61.
[40] Meng F, Henson R, Lang M, Wehbe H, Maheshwari S, Mendell JT, et al. Involvement of human micro-RNA in growth and response to chemotherapy in human cholangiocarcinoma cell lines. Gastroenterology 2006;130:2113–29.
[41] Hanash S. Disease proteomics. Nature 2003;422:226–32.
[42] Qu Y, Yang Y, Liu B, Xiao W. Comparative proteomic profiling identified sorcin being associated with gemcitabine resistance in non-small cell lung cancer. Med Oncol 2010;27:1303–8.
[43] Dabiri GA, Young CL, Rosenbloom J, Southwick FS. Molecular cloning of human macrophage capping protein cDNA. A unique member of the gelsolin/villin family expressed primarily in macrophages. J Biol Chem 1992;267: 16545–52.
[44] Renz M, Langowski J. Dynamics of the CapG actin-binding protein in the cell nucleus studied by FRAP and FCS. Chromosome Res 2008;16:427–37.
[45] Voskoglou-Nomikos T, Pater JL, Seymour L. Clinical predictive value of the in vitro cell line, human xenograft, and mouse allograft preclinical cancer models. Clin Cancer Res 2003;9: 4227–39.

Cell Metabolism
Article

The FBXL5-IRP2 Axis Is Integral to Control of Iron Metabolism In Vivo

Toshiro Moroishi,[1,2] Masaaki Nishiyama,[1,2] Yukiko Takeda,[2,3] Kazuhiro Iwai,[2,3] and Keiichi I. Nakayama[1,2,*]
[1]Department of Molecular and Cellular Biology, Medical Institute of Bioregulation, Kyushu University, 3-1-1 Maidashi, Higashi-ku, Fukuoka, Fukuoka 812-8582, Japan
[2]CREST, Japan Science and Technology Agency (JST), Kawaguchi, Saitama 332-0012, Japan
[3]Department of Biophysics and Biochemistry, Graduate School of Medicine, and Cell Biology and Metabolism Group, Graduate School of Frontier Biosciences, Osaka University, Suita, Osaka 565-0871, Japan
*Correspondence: nakayak1@bioreg.kyushu-u.ac.jp
DOI 10.1016/j.cmet.2011.07.011

SUMMARY

Iron-dependent degradation of iron-regulatory protein 2 (IRP2) is a key event for maintenance of an appropriate intracellular concentration of iron. Although FBXL5 (F box and leucine-rich repeat protein 5) is thought to mediate this degradation, the role of FBXL5 in the control of iron homeostasis in vivo has been poorly understood. We have now found that mice deficient in FBXL5 died in utero, associated with excessive iron accumulation. This embryonic mortality was prevented by additional ablation of IRP2, suggesting that impaired IRP2 degradation is primarily responsible for the death of *Fbxl5*$^{-/-}$ mice. We also found that liver-specific deletion of *Fbxl5* resulted in deregulation of both hepatic and systemic iron homeostasis, leading to the development of steatohepatitis. The liver-specific mutant mice died with acute liver failure when fed a high-iron diet. Thus, our results uncover a major role for FBXL5 in ensuring an appropriate supply of iron to cells.

INTRODUCTION

Iron is an essential cofactor for many proteins that function in oxygen transport, cellular respiration, or DNA synthesis (Rouault and Tong, 2005), with iron deficiency resulting in cellular growth arrest and death. Conversely, the chemical properties of iron give rise to side reactions that damage macromolecules (Hentze et al., 2010). Thus, excess ferrous iron reacts with hydrogen peroxide or lipid peroxides to generate hydroxyl and lipid radicals, respectively. These oxygen metabolites react readily with biological molecules including proteins, lipids, and DNA. Given that both iron deficiency and iron overload are deleterious to cells, defects in iron acquisition at the cellular and systemic levels lead to human disorders (De Domenico et al., 2008). Thus, iron homeostasis is strictly controlled to ensure provision of a proper amount of iron to cells.

The control of systemic iron homeostasis occurs through regulation of iron acquisition (Andrews and Schmidt, 2007), given that iron loss occurs only through exfoliation and blood loss. Plasma iron levels are determined predominantly by the amount of duodenal iron absorption and by iron release from macrophages that recycle iron from senescent red blood cells (Wang and Pantopoulos, 2011). These iron fluxes are precisely regulated by hepcidin, a small peptide hormone released from the liver that is also known as Hamp1 or Leap1. Hepcidin negatively regulates iron transport into plasma by controlling the expression of an iron exporter, ferroportin (Nemeth et al., 2004). Thus, systemic iron metabolism is maintained in balance by the hepcidin-ferroportin regulatory system.

At the cellular level, iron homeostasis is regulated by coordination of iron uptake, storage, export, and utilization (Hentze et al., 2010). Iron is imported into cells in the ferrous form and accumulates as a cytosolic labile iron pool (LIP) that is essential for direct incorporation of iron into proteins or for its transport into mitochondria, which constitute a major site of iron utilization. Ferrous iron from the LIP that is not utilized for metalation reactions is exported by ferroportin or stored in a redox-inactive form (ferric iron) bound to ferritin, thereby preventing iron-mediated cell damage. Thus, the size of the LIP is determined by the rates of iron uptake, storage, export, and utilization, and these processes must be strictly regulated to prevent deleterious iron deficiency or excess.

The abundance of some proteins that contribute to determination of the size of the LIP is regulated at the posttranscriptional level by iron-regulatory protein 1 (IRP1) and IRP2 (Muckenthaler et al., 2008). These RNA-binding proteins interact with conserved *cis*-regulatory hairpin structures known as iron-responsive elements (IREs) during iron-limiting conditions to regulate the translation and stability of mRNAs that encode proteins required for iron homeostasis. IRP1 (but not IRP2) is a bifunctional protein: in the apo-IRP1 form, it binds to IREs and thereby controls gene expression; however, it also assembles to form a [4Fe-4S] cluster that does not bind IREs and thereby becomes cytosolic aconitase (holo-IRP1) under iron-sulfur cluster-replete conditions. Both apo-IRP1 and IRP2 inhibit initiation of translation when they are bound to IREs in the 5′ untranslated regions of mRNAs for the H or L chains of ferritin (which mediate iron storage), for ferroportin (which mediates iron export), or for aminolevulinic acid synthase 2 (Alas2, which mediates iron utilization), whereas their binding to the IRE in the 3′ untranslated region of the mRNA for transferrin receptor 1 (TfR1, which mediates iron uptake) prevents its degradation.

As a consequence of these interactions, IRPs increase the size of the LIP (ferrous iron) during iron-limiting conditions. In contrast, under iron-replete conditions, IRPs are degraded by the proteasome, leading to a decrease in the size of the cytosolic LIP. Thus, iron-dependent degradation of IRPs in iron-replete cells is a key event in the maintenance of an appropriate intracellular concentration of iron.

An iron- and oxygen-regulated SCF-type ubiquitin ligase (E3), SCF^{FBXL5}, has been shown to contribute to iron-dependent degradation of IRP1 and IRP2 (Salahudeen et al., 2009; Vashisht et al., 2009). FBXL5 (F box and leucine-rich repeat protein 5) is a member of the F box family of proteins that confer substrate specificity on SCF-type ubiquitin ligases (Jin et al., 2004; Nakayama and Nakayama, 2006). FBXL5 contains a unique hemerythrin domain that is related to a family of iron- and oxygen-binding proteins in bacteria and invertebrates. Direct binding of iron to the hemerythrin domain stabilizes FBXL5, which is unstable under iron-deficient conditions. Thus, such binding results in the degradation of IRPs by the stabilized FBXL5 under iron-replete conditions. However, despite its integral role in IRP degradation, the biological relevance of FBXL5 as well as its effects on iron homeostasis have remained unknown.

We have now inactivated the mouse FBXL5 gene globally and selectively. Our characterization of these FBXL5-deficient mice has revealed that FBXL5 plays a pivotal role in the maintenance of appropriate concentrations of intracellular iron and that it is essential both for embryonic development and for normal postnatal liver physiology. Loss of FBXL5 in mice induced apoptosis as a result of unrestrained IRP activity, and consistent with this finding, deletion of *Irp2* in $Fbxl5^{-/-}$ mice prevented their embryonic death. Our results indicate that the FBXL5-IRP2 axis is integral to iron homeostasis in vivo.

RESULTS

Loss of FBXL5 Results in Embryonic Mortality in Mice

To elucidate the physiological functions of FBXL5, we generated mice deficient in this protein. The FBXL5 gene was disrupted in mouse embryonic stem cells (ESCs) by replacement of exons 4 and 5, which encode the F box domain, with IRES-*lacZ* and PGK-*neo*-poly(A)-loxP cassettes (see Figure S1 available online). Mice heterozygous for the *Fbxl5* mutant allele were healthy, fertile, and phenotypically indistinguishable from wild-type littermates. In contrast no homozygous mutants were detected among 372 newborn animals generated from heterozygote crosses, even though the ratio of wild-type to heterozygous offspring was normal (Figure 1A). Thus, the mutation appeared to be embryonic lethal in the homozygous state. Whole-mount in situ hybridization analysis revealed that FBXL5 mRNA was present throughout wild-type embryos from embryonic day (E) 7.5 to E8.5 but that it was localized predominantly in the brain from E9.5 to E11.5 (Figure 1B). No hybridization signal was detected in $Fbxl5^{-/-}$ embryos (Figure 1C).

To determine the time at which the *Fbxl5* mutation becomes lethal, we examined embryos from $Fbxl5^{+/-}$ intercrosses at various developmental stages (Figure 1A). Most $Fbxl5^{-/-}$ embryos underwent resorption manifesting growth retardation and massive hemorrhage at E8.5 and thereafter, although the mutant embryos appeared normal at E7.5 (Figure 1D). Histopathologic examination revealed that $Fbxl5^{+/-}$ and $Fbxl5^{-/-}$ embryos were indistinguishable at E7.5, with each egg cylinder consisting of three layers of tissue (ectoderm, mesoderm, and visceral endoderm) (Figure 1E). However, $Fbxl5^{-/-}$ embryos manifested growth retardation and were inviable at E8.5. Apoptotic cells with condensed nuclei as well as hemorrhage in the region of the ectoplacental cone were typically observed in the $Fbxl5^{-/-}$ embryos. Thus, these results suggested that FBXL5 is essential for early embryonic development.

Fatal Iron Accumulation in $Fbxl5^{-/-}$ Embryos

To explore the cause of the abnormal cell death observed in the ectoplacental cone of $Fbxl5^{-/-}$ embryos, we performed diaminobenzidine (DAB)-enhanced Perls staining and DAB-enhanced Turnbull staining, which are specific for ferric and ferrous iron, respectively (Meguro et al., 2003) (Figure 2A). Both Perls- and Turnbull-positive iron deposits were observed in the ectoplacental cone of $Fbxl5^{-/-}$ embryos at E8.5, suggesting that ferrous iron accumulated in these embryos. Furthermore, ferrous iron deposits were also observed in the extraembryonic visceral endoderm of $Fbxl5^{-/-}$ embryos at E7.5, before morphological changes were apparent.

The extraembryonic visceral endoderm and the ectoplacental cone function as an early placenta in maternoembryonic nutrient transport before formation of the placenta proper (Cross et al., 1994). Given that iron is supplied to the embryo through this early placenta, we hypothesized that the loss of FBXL5 might result in iron overload in the early placenta, leading to oxidative stress. A marked increase in the abundance of cytoplasmic 4-hydroxy-2-nonenal (4-HNE)-modified proteins, an indicator of oxidative stress, was apparent as early as E7.5 in the extraembryonic visceral endoderm of $Fbxl5^{-/-}$ embryos, compared with that in $Fbxl5^{+/-}$ embryos (Figure 2B). Although the TUNEL (terminal deoxynucleotidyl transferase-mediated dUTP nick-end labeling) assay did not detect apoptotic cells at E7.5 (Figure S2A), several apoptotic cells were apparent in the ectoplacental cone as well as in the embryonic portion of $Fbxl5^{-/-}$ embryos at E8.5 (Figure 2C). These results suggested that the loss of FBXL5 results in iron overload, leading to oxidative stress and apoptosis, in the early embryo.

To assess directly the growth capability of $Fbxl5^{-/-}$ embryos independent of placental function, we examined the outgrowth of blastocysts in culture. All $Fbxl5^{+/+}$, $Fbxl5^{+/-}$, and $Fbxl5^{-/-}$ blastocysts hatched, attached to the culture dish, and produced apparently normal trophoblast giant cells and an inner cell mass under normal iron conditions (Figure S2B), suggesting that $Fbxl5^{-/-}$ blastocysts develop normally in the absence of iron stress. However, under high-iron conditions, development of both the trophectoderm and inner cell mass by $Fbxl5^{-/-}$ blastocysts was impaired, with this impairment being prevented by the presence of the antioxidant *N*-acetyl-L-cysteine (NAC) (Figure 2D). Thus, these observations indicated that not only the early placenta but also embryonic tissue is damaged by iron overload and consequent oxidative stress in the absence of FBXL5.

IRP Accumulation in FBXL5-Deficient Mice

Given that iron accumulation was observed in $Fbxl5^{-/-}$ embryos, we hypothesized that upregulation of IRPs might be

A

Embryonic day	No. of animals recoverable			Total no. of animals
	Fbxl5$^{+/+}$	*Fbxl5*$^{+/-}$	*Fbxl5*$^{-/-}$ (no. resorbed)	
E3.5	3	12	6 (0)	21
E7.5	18	29	9 (0)	56
E8.5	11	19	4 (4)	34
E9.5	4	17	7 (7)	28
E11.5	8	14	8 (8)	30
E13.5	15	33	12 (12)	60
Newborn	132	240	0 (0)	372

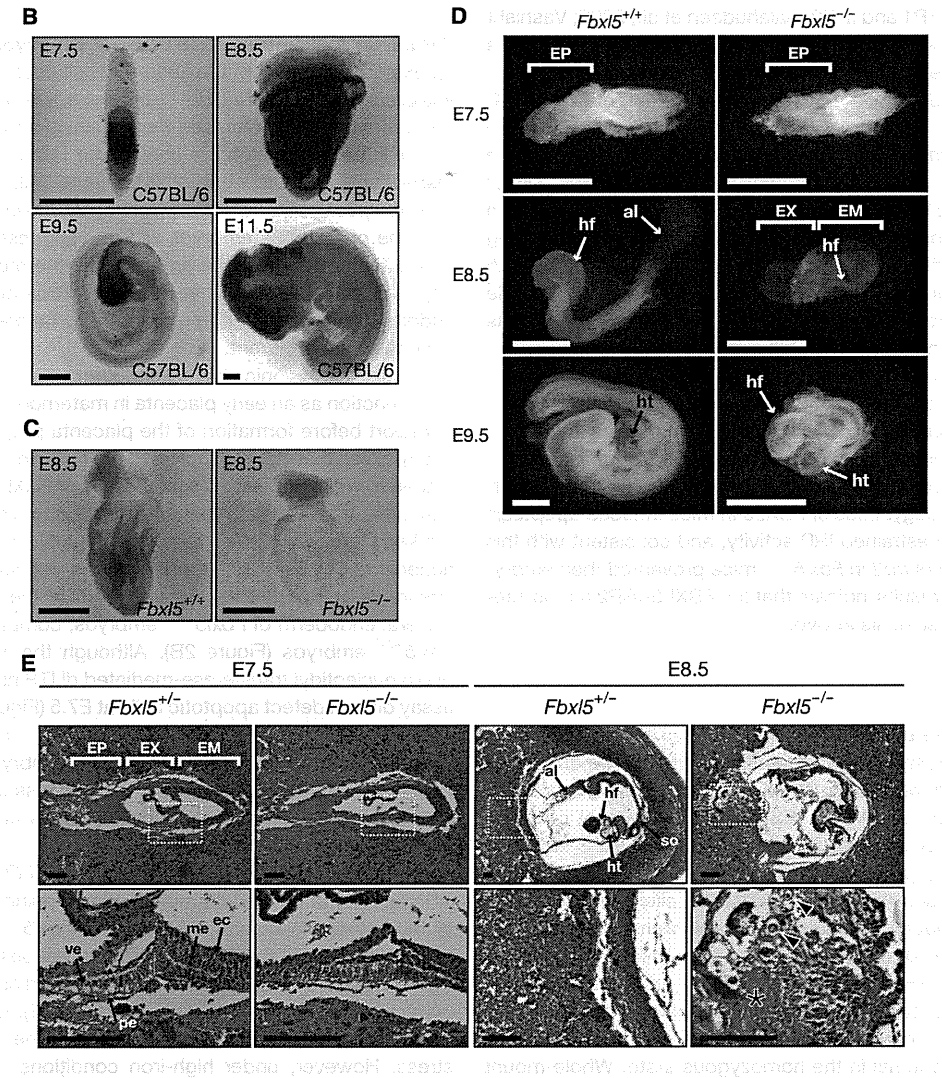

Figure 1. Targeted Disruption of *Fbxl5* Results in Embryonic Death

(A) Genotype frequencies for total embryos and live offspring produced from *Fbxl5*$^{+/-}$ mouse intercrosses. Numbers in parentheses indicate resorbed embryos.

(B) Whole-mount in situ hybridization of C57BL/6 embryos at E7.5, E8.5, E9.5, and E11.5 with a riboprobe specific for FBXL5 mRNA. Scale bars, 500 μm.

(C) Whole-mount in situ hybridization of *Fbxl5*$^{+/+}$ and *Fbxl5*$^{-/-}$ embryos at E8.5 with an FBXL5 riboprobe. Scale bars, 500 μm.

(D) Gross appearance of *Fbxl5*$^{+/+}$ versus *Fbxl5*$^{-/-}$ embryos at E7.5, E8.5, and E9.5. EP, ectoplacental cone; EX, extraembryonic portion; EM, embryonic portion; hf, headfold; al, allantois; ht, heart. Scale bars, 500 μm.

(E) Histopathology of *Fbxl5*$^{-/-}$ embryos. The development of *Fbxl5*$^{+/-}$ and *Fbxl5*$^{-/-}$ embryos is shown at E7.5 and E8.5. The boxed regions in the upper panels are shown at higher magnification in the lower panels. Apoptotic cells with condensed nuclei (arrowheads) as well as hemorrhage and fibrin (asterisk) in the area of the ectoplacental cone are indicated. ec, ectoderm; me, mesoderm; pe, parietal endoderm; ve, visceral endoderm; so, somites. Scale bars, 100 μm. See also Figure S1.

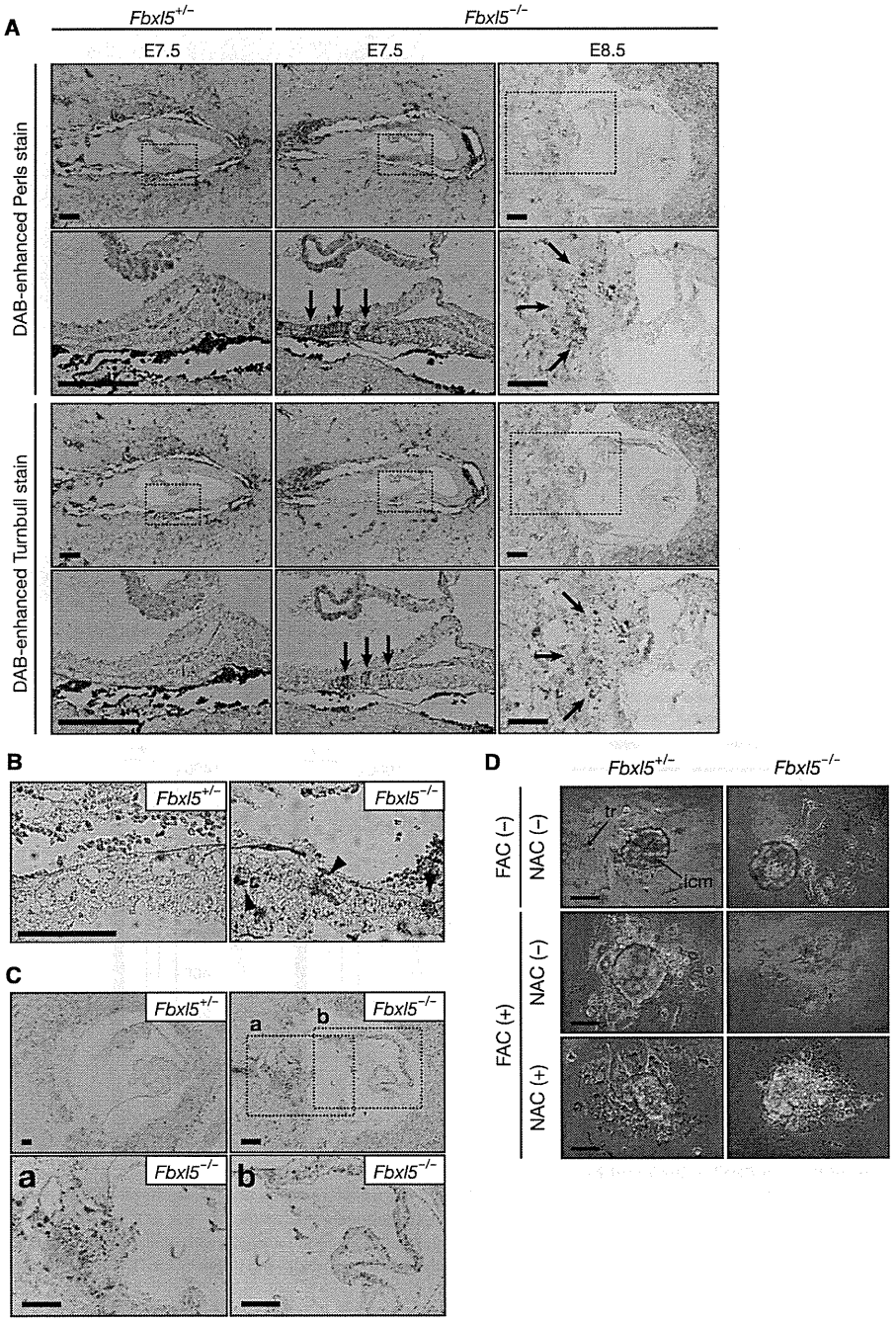

Figure 2. Fatal Iron Accumulation and Oxidative Stress in *Fbxl5*$^{-/-}$ Embryos

(A) DAB-enhanced Perls staining (top panels) and DAB-enhanced Turnbull staining (bottom panels) of *Fbxl5*$^{+/-}$ (E7.5) and *Fbxl5*$^{-/-}$ (E7.5 and E8.5) embryos. The boxed regions in the upper panels of each set are shown at higher magnification in the lower panels. Brown staining indicates iron accumulation in the extra-embryonic visceral endoderm (E7.5) or ectoplacental cone (E8.5) of *Fbxl5*$^{-/-}$ embryos (arrows). Scale bars, 100 μm.

(B) Sections of *Fbxl5*$^{+/-}$ and *Fbxl5*$^{-/-}$ embryos at E7.5 were subjected to immunohistochemical staining with antibodies to 4-HNE. Arrowheads indicate an increased staining intensity for 4-HNE-modified proteins in the extraembryonic visceral endoderm of the *Fbxl5*$^{-/-}$ embryo. Scale bar, 50 μm.

(C) Sections of *Fbxl5*$^{+/-}$ and *Fbxl5*$^{-/-}$ embryos at E8.5 were subjected to the TUNEL assay. Higher-magnification views of the ectoplacental cone (a) and embryonic portion (b) of the *Fbxl5*$^{-/-}$ embryo are also shown. Scale bars, 100 μm.

(D) Blastocysts from *Fbxl5*$^{+/-}$ mouse intercrosses were cultured in the absence or presence of ferric ammonium citrate (FAC, 50 μg/ml) or NAC (1 mM) for 5 days in vitro. The development of *Fbxl5*$^{+/-}$ and *Fbxl5*$^{-/-}$ blastocysts was examined at E8.5. icm, inner cell mass; tr, trophectoderm. Scale bars, 100 μm. See also Figure S2.

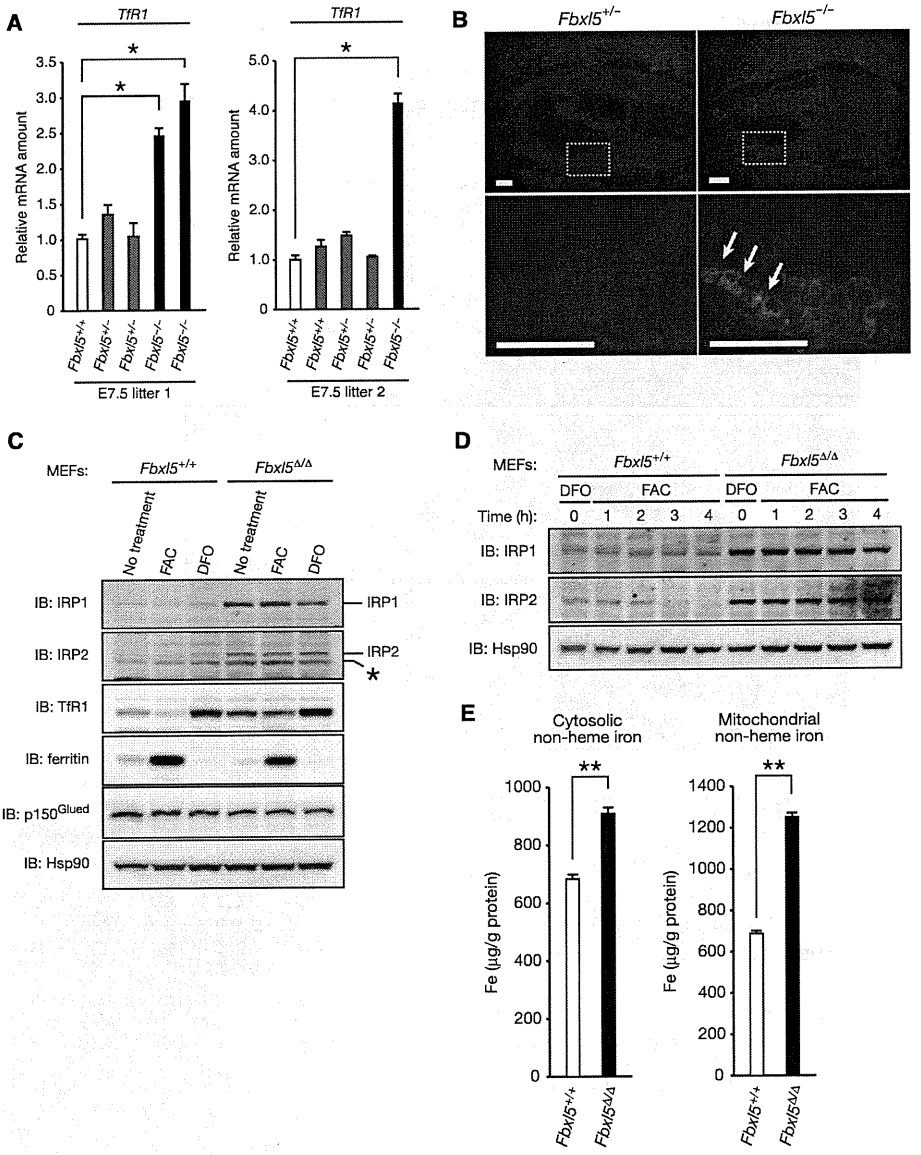

Figure 3. Accumulation of IRPs in FBXL5-Deficient Mice

(A) RT and real-time PCR analysis of TfR1 mRNA in littermate embryos of *Fbxl5*$^{+/-}$ mouse intercrosses at E7.5. Normalized data are expressed relative to the corresponding value for a control *Fbxl5*$^{+/+}$ embryo and are mean ± SEM from three independent experiments. *$p < 0.03$ (Student's t test).

(B) Sections of *Fbxl5*$^{+/-}$ and *Fbxl5*$^{-/-}$ embryos at E7.5 were subjected to immunohistofluorescence analysis with antibodies to TfR1. The boxed regions in the upper panels are shown at higher magnification in the lower panels. Arrows indicate an increased staining intensity for TfR1 in the extraembryonic mesoderm of the *Fbxl5*$^{-/-}$ embryo. Scale bars, 50 μm.

(C) *Fbxl5*$^{+/+}$ or *Fbxl5*$^{\Delta/\Delta}$ MEFs were incubated for 16 hr in the absence or presence of FAC (100 μg/ml) or 100 μM of the ferric-iron chelator desferrioxamine (DFO) and were then subjected to immunoblot (IB) analysis with antibodies to the indicated proteins. The asterisk indicates a nonspecific band.

(D) Immunoblot analysis of IRP1 and IRP2 in cells exposed to iron. *Fbxl5*$^{+/+}$ or *Fbxl5*$^{\Delta/\Delta}$ MEFs were incubated for 16 hr with 100 μM DFO and then exposed to FAC (50 μg/ml) for the indicated times.

(E) Total nonheme iron levels in cytosolic and mitochondrial fractions prepared from *Fbxl5*$^{+/+}$ or *Fbxl5*$^{\Delta/\Delta}$ MEFs that had been exposed to FAC (100 μg/ml) for 48 hr. Data are mean ± SD from three independent experiments. **$p < 0.01$ (Student's t test). See also Figure S3.

responsible for this deregulation of iron homeostasis. Therefore, we examined the abundance of TfR1 mRNA, a downstream target of IRPs, in the mutant embryos. The amount of TfR1 mRNA was markedly increased in *Fbxl5*$^{-/-}$ embryos (Figure 3A). Immunostaining also revealed that TfR1 accumulated in the extraembryonic mesoderm of *Fbxl5*$^{-/-}$ embryos at E7.5 (Figure 3B). Thus, these results suggested that IRP activity is increased, resulting in deregulation of IRP target genes, in *Fbxl5*$^{-/-}$ embryos.

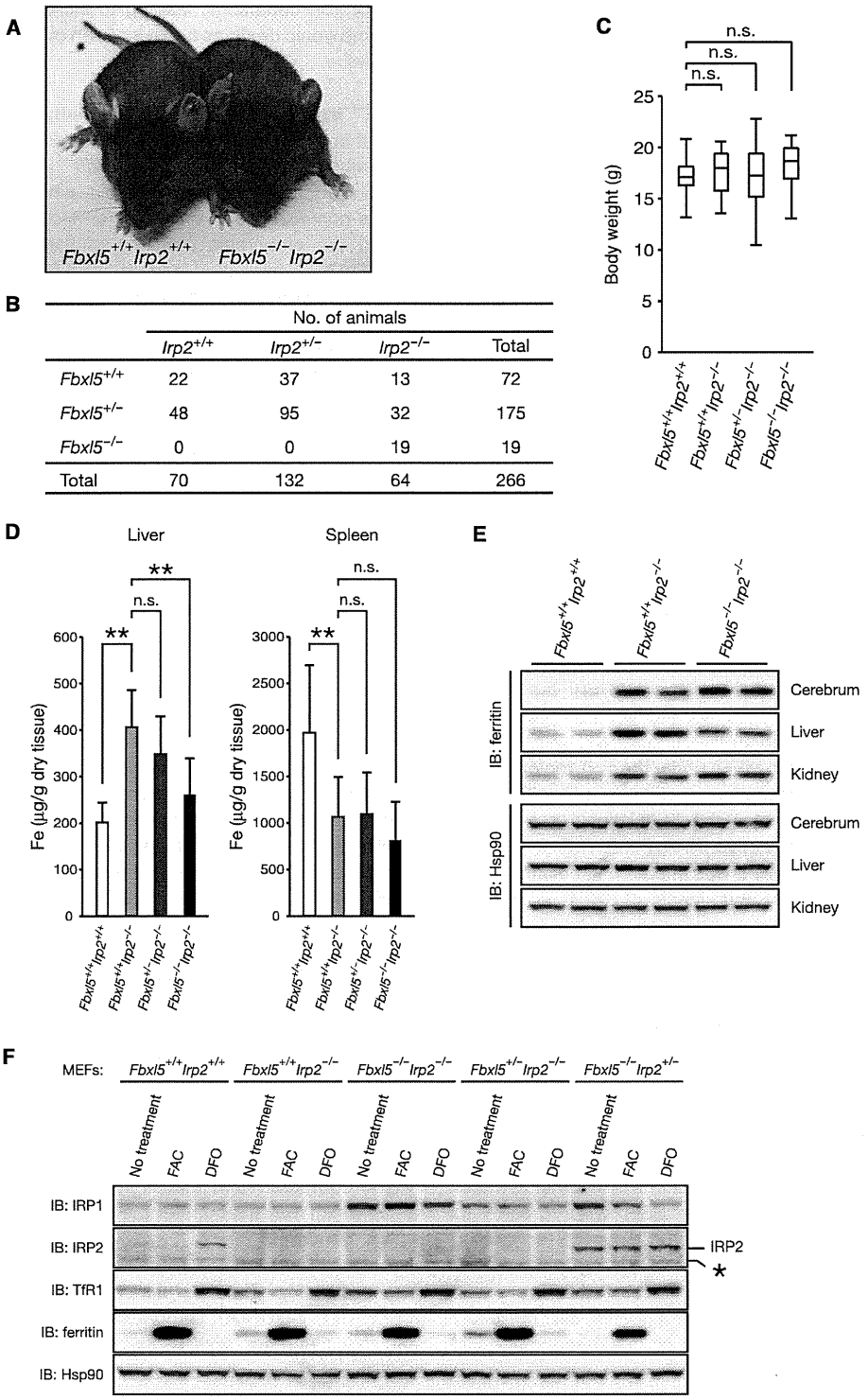

Figure 4. Prevention of Embryonic Mortality in FBXL5-Deficient Mice by Ablation of IRP2

(A) Gross appearance of *Fbxl5*$^{+/+}$*Irp2*$^{+/+}$ versus *Fbxl5*$^{-/-}$*Irp2*$^{-/-}$ littermates at 5 weeks of age.

(B) Genotype frequencies of 4-week-old mice produced from *Fbxl5*$^{+/-}$*Irp2*$^{+/-}$ mouse intercrosses.

(C) Box plot with whiskers from minimum to maximum body weight in *Fbxl5*$^{+/+}$*Irp2*$^{+/+}$ (n = 22), *Fbxl5*$^{+/+}$*Irp2*$^{-/-}$ (n = 10), *Fbxl5*$^{+/-}$*Irp2*$^{-/-}$ (n = 26), and *Fbxl5*$^{-/-}$*Irp2*$^{-/-}$ (n = 15) mice at 4 weeks of age. n.s., not significant ($p > 0.05$, Student's t test).

The early embryonic mortality of the *Fbxl5*$^{-/-}$ mutant impeded in-depth analysis of the role of FBXL5 in iron homeostasis. To overcome this obstacle, we generated mice in which *Fbxl5* is conditionally ablated in a tissue-specific manner. To this end, we first produced mice harboring a "floxed" allele of *Fbxl5*, in which exons 4 and 5 are flanked by loxP sites (Figures S3A–S3C). Mice homozygous for the floxed *Fbxl5* allele (*Fbxl5*$^{F/F}$ mice) had no apparent defects, indicating that the allele is fully functional.

To investigate whether iron-dependent degradation of IRPs is impaired in FBXL5-deficient mice, we prepared mouse embryonic fibroblasts (MEFs) from *Fbxl5*$^{+/+}$ and *Fbxl5*$^{F/F}$ embryos at E13.5 and subsequently infected these cells with a retroviral vector encoding Cre recombinase. We confirmed that almost all floxed alleles were deleted by Cre recombinase in the MEFs from *Fbxl5*$^{F/F}$ embryos, giving rise to *Fbxl5*$^{\Delta/\Delta}$ MEFs (Figure S3D). Immunoblot analysis revealed that the abundance of IRP1 and IRP2 was increased in *Fbxl5*$^{\Delta/\Delta}$ MEFs, whereas that of the other potential substrate of FBXL5, p150^{Glued} (Zhang et al., 2007), was not (Figure 3C). Such IRP accumulation was apparent even under iron-replete conditions. Consistent with this finding, the expression of proteins encoded by mRNA targets of IRPs was also deregulated: thus, the abundance of TfR1 (which mediates iron uptake) was increased, whereas that of ferritin (which mediates iron storage) was decreased likely as a result of IRP-mediated translational suppression (Figure 3C). However, the transcription of ferritin genes is also regulated by oxidative stress through an antioxidant-responsive element (ARE) in the 5′ region (MacKenzie et al., 2008). Indeed, the expression of ferritin was markedly increased at both mRNA (Figure S3E) and protein (Figure 3C) levels in *Fbxl5*$^{\Delta/\Delta}$ MEFs under the iron-replete condition, suggesting that transcriptional activation of ferritin genes by oxidative stress dominates the translational suppression mediated by constitutively active IRPs. Furthermore, the iron-dependent degradation of IRP2 was impaired in *Fbxl5*$^{\Delta/\Delta}$ MEFs (Figure 3D). Although the abundance of IRP1 in *Fbxl5*$^{\Delta/\Delta}$ MEFs was markedly increased compared with that in *Fbxl5*$^{+/+}$ MEFs, the half-life of this protein was long even in iron-replete *Fbxl5*$^{+/+}$ MEFs (Figure 3D), probably reflecting the fact that most IRP1s exist in the holo-IRP1 form, which is resistant to degradation in iron-replete cells (Recalcati et al., 2006). These results suggested that IRPs accumulate, resulting in an increase in total IRP activity, in FBXL5-deficient embryos and MEFs in a manner independent of iron conditions, leading to deregulation of IRP targets.

We next examined how such IRP hyperactivation affects cellular iron homeostasis. The levels of iron in isolated cytosolic and mitochondrial fractions (Figure S3F) were greater for *Fbxl5*$^{\Delta/\Delta}$ MEFs than for *Fbxl5*$^{+/+}$ MEFs (Figure 3E), suggesting that the accumulated IRPs promote iron loading in the cytosol and mitochondria, leading to oxidative stress, in the former cells. Thus, collectively, our observations suggested that the abundance and activity of IRPs are increased in a manner independent of iron conditions, leading to increased oxidative stress and embryonic death as a result of iron overload, in FBXL5-deficient mice.

Fbxl5$^{-/-}$*Irp2*$^{-/-}$ Mice Develop Normally

To test our hypothesis that IRP accumulation is responsible for the early embryonic death of *Fbxl5*$^{-/-}$ mice, we examined whether additional ablation of IRP2, which dominates control of iron homeostasis in vivo (Meyron-Holtz et al., 2004b), prevented the embryonic mortality of these animals. Whereas most *Fbxl5*$^{-/-}$ mice died in utero at E8.5, *Fbxl5*$^{-/-}$*Irp2*$^{-/-}$ mice developed normally and were fertile (Figures 4A and 4B). *Fbxl5*$^{-/-}$*Irp2*$^{-/-}$ mice were macroscopically indistinguishable from wild-type littermates and grew normally (Figure 4C).

Iron metabolism in *Fbxl5*$^{-/-}$*Irp2*$^{-/-}$ mice appeared almost identical to that in *Irp2*$^{-/-}$ mice, with some exceptions. *Irp2*$^{-/-}$ mice manifest mild microcytic anemia and an abnormal distribution of iron within the body, including iron accumulation in the liver and a reduced iron level in the spleen (Cooperman et al., 2005; Galy et al., 2005). The hematocrit and serum concentration of hemoglobin were significantly reduced in *Irp2*$^{-/-}$ mice in association with a normal erythrocyte count and a lower mean cell volume (Table 1). The hematologic parameters of *Fbxl5*$^{-/-}$*Irp2*$^{-/-}$ mice were indistinguishable from those of *Irp2*$^{-/-}$ mice. However, the serum iron concentration as well as transferrin saturation were increased in *Fbxl5*$^{-/-}$*Irp2*$^{-/-}$ mice, whereas these parameters did not differ between *Irp2*$^{-/-}$ and wild-type mice (Table 1). Although the precise mechanism underlying these paradoxical increases remains unknown, these results suggest that the microcytosis in *Fbxl5*$^{-/-}$*Irp2*$^{-/-}$ mice is not attributable to systemic iron deficiency. We also measured organ nonheme iron content and found that it was increased in the liver and decreased in the spleen of *Irp2*$^{-/-}$ mice, consistent with previous observations, whereas the liver iron content of *Fbxl5*$^{-/-}$*Irp2*$^{-/-}$ mice was significantly decreased compared with that of *Irp2*$^{-/-}$ mice (Figure 4D). Immunoblot analysis revealed that the abundance of ferroportin was not significantly changed in the liver of *Fbxl5*$^{-/-}$*Irp2*$^{-/-}$ mice (Figure S4A). The expression of the iron-storage protein ferritin was increased in the cerebrum, liver, and kidney of *Irp2*$^{-/-}$ mice (Figure 4E). However, the abundance of ferritin in the liver of *Fbxl5*$^{-/-}$*Irp2*$^{-/-}$ mice was decreased compared with that in *Irp2*$^{-/-}$ mice, mirroring the decrease in iron content. An electrophoretic mobility shift assay (EMSA) revealed that the IRE-binding activity of IRP1 in the liver of *Fbxl5*$^{-/-}$*Irp2*$^{-/-}$ mice was increased by ~20% compared with that in *Irp2*$^{-/-}$ mice (Figures S4B and S4C), which may account for the decreased ferritin level.

We generated *Fbxl5*$^{-/-}$*Irp2*$^{-/-}$ MEFs and analyzed the response of iron-related proteins in these cells to changes in iron availability. The abundance of IRP1 in *Fbxl5*$^{-/-}$*Irp2*$^{-/-}$ MEFs was increased compared with that in *Irp2*$^{-/-}$ MEFs, and this difference was associated with a slight increase in

(D) Nonheme iron content of the liver and spleen of *Fbxl5*$^{+/+}$*Irp2*$^{+/+}$ (n = 8), *Fbxl5*$^{+/+}$*Irp2*$^{-/-}$ (n = 8), *Fbxl5*$^{+/-}$*Irp2*$^{-/-}$ (n = 10), and *Fbxl5*$^{-/-}$*Irp2*$^{-/-}$ (n = 12) mice at 9–13 weeks of age. Data are mean ± SD. **p < 0.01 (Student's t test).

(E) Immunoblot analysis of extracts of the cerebrum, liver, and kidney of 11-week-old mice of the indicated genotypes with antibodies to ferritin and to Hsp90. Two animals were examined for each genotype.

(F) Primary cultured MEFs of the indicated genotypes were incubated for 16 hr in the absence or presence of FAC (100 μg/ml) or 100 μM DFO and were then subjected to immunoblot analysis with antibodies to the indicated proteins. The asterisk indicates a nonspecific band. See also Figure S4.

Table 1. Hematologic and Serum Iron Parameters of *Fbxl5*$^{-/-}$*Irp2*$^{-/-}$ Mice

Hematologic Parameters				
Parameter	*Fbxl5*$^{+/+}$*Irp2*$^{+/+}$ (n = 11)	*Fbxl5*$^{+/+}$*Irp2*$^{-/-}$ (n = 8)	*Fbxl5*$^{+/-}$*Irp2*$^{-/-}$ (n = 11)	*Fbxl5*$^{-/-}$*Irp2*$^{-/-}$ (n = 15)
RBC count (10^4/μl)	1000 ± 37.8	952 ± 60.1	998 ± 55.4	985 ± 40.0
MCV (fl)	52.4 ± 0.6	49.3 ± 0.7[a]	48.9 ± 1.1[a]	48.7 ± 1.0[a]
Hematocrit (%)	52.4 ± 2.2	47.0 ± 3.2[a]	48.6 ± 2.5[a]	48.0 ± 1.9[a]
Serum hemoglobin (g/dl)	15.9 ± 0.7	13.7 ± 0.9[a]	14.3 ± 0.7[a]	14.0 ± 0.5[a]
MCH (pg)	15.9 ± 0.2	14.4 ± 0.4[a]	14.3 ± 0.5[a]	14.2 ± 0.3[a]
MCHC (g/dl)	30.3 ± 0.3	29.3 ± 0.5[a]	29.3 ± 0.5[a]	29.2 ± 0.5[a]
Serum Iron Parameters				
Parameter	*Fbxl5*$^{+/+}$*Irp2*$^{+/+}$ (n = 6)	*Fbxl5*$^{+/+}$*Irp2*$^{-/-}$ (n = 6)	*Fbxl5*$^{+/-}$*Irp2*$^{-/-}$ (n = 6)	*Fbxl5*$^{-/-}$*Irp2*$^{-/-}$ (n = 8)
TIBC (μg/dl)	366 ± 26. 4	359 ± 44.4	398 ± 36.9	334 ± 36.6
Iron (μg/dl)	150 ± 33.1	152 ± 32.6	163 ± 30.7	209 ± 33.5[a]
Transferrin saturation (%)	41.4 ± 11.1	42.5 ± 8.8	41.0 ± 8.8	63.9 ± 15.2[a]

Data are mean ± SD for the indicated numbers of 9- to 13-week-old mice. Transferrin saturation was calculated from measured serum iron and TIBC. RBC, red blood cell; MCV, mean cell volume; MCH, mean corpuscular hemoglobin; MCHC, mean corpuscular hemoglobin concentration; TIBC, total iron-binding capacity.
[a] $p < 0.01$ versus *Fbxl5*$^{+/+}$*Irp2*$^{+/+}$ mice (Student's t test).

TfR1 expression under iron-replete conditions (Figure 4F). These observations suggested that IRP1 activity was slightly increased in *Fbxl5*$^{-/-}$*Irp2*$^{-/-}$ mice. Thus, we concluded that the increased activity of IRP1 in *Fbxl5*$^{-/-}$*Irp2*$^{-/-}$ mice attenuated the increased hepatic levels of iron and ferritin apparent in *Irp2*$^{-/-}$ mice.

Liver-Specific Ablation of *Fbxl5*

To study the function of FBXL5 in adult mouse tissues, we next examined the consequences of FBXL5 deficiency in the liver, which plays a central role in systemic iron homeostasis. To ablate *Fbxl5* in the liver, we crossed *Fbxl5*$^{F/F}$ mice with mice harboring a Cre transgene under the control of the promoter for the albumin gene (*Alb*-Cre mice). We confirmed that almost all floxed alleles were inactivated by Cre recombinase in the liver of *Alb*-Cre/*Fbxl5*$^{F/F}$ mice, as revealed by a corresponding decrease in the amount of FBXL5 mRNA (Figure S5A). *Alb*-Cre/*Fbxl5*$^{F/F}$ mice were viable, but the liver of these animals was lighter in color compared with that of their *Alb*-Cre/*Fbxl5*$^{F/+}$ littermates (Figure 5A). Histological analysis revealed that the nuclei of cells in the liver of *Alb*-Cre/*Fbxl5*$^{F/F}$ mice remained centrally located, whereas the corresponding cytoplasm was only weakly eosinophilic and contained numerous microvesicular vacuoles (Figures 5B and 5C). Lobular infiltration of inflammatory cells such as lymphocytes and neutrophils was also observed in the liver of *Alb*-Cre/*Fbxl5*$^{F/F}$ mice (Figure 5D), indicative of hepatic inflammation. However, serum chemistry parameters associated with liver damage did not differ between the mutant and control mice under normal fed conditions (Table S1), indicating that the hepatic inflammation in the mutant animals is mild. Oil red O staining revealed deposition of multiple small lipid droplets with an undisplaced nucleus in liver cells of the mutant mice (Figures 5E and 5F), a characteristic of liver damage associated with impaired mitochondrial function (Burt, 2001). Consistent with mitochondrial dysfunction, ATP levels of *Fbxl5*$^{\Delta/\Delta}$ MEFs under basal conditions were reduced compared with those of *Fbxl5*$^{+/+}$ MEFs, and this reduction was further enhanced under high-iron conditions (Figure S5B). Moreover, electron microscopy revealed mitochondriopathy associated with small lipid droplets in FBXL5-deficient hepatocytes; the mitochondria were swollen, with a hypodense matrix suggestive of mitochondrial injury (Figures 5G–5J).

We next examined iron metabolism in *Alb*-Cre/*Fbxl5*$^{F/F}$ mice. DAB-enhanced Perls and Turnbull staining revealed the accumulation of ferrous iron in hepatocytes of *Alb*-Cre/*Fbxl5*$^{F/F}$ mice (Figures 5K–5N). Immunoblot analysis showed that IRP2 also accumulated in the liver of these mice (Figure 5O). The abundance of IRP1 was also increased in the liver of *Alb*-Cre/*Fbxl5*$^{F/F}$ mice, but the extent of this change was much less pronounced than was that observed in *Fbxl5*$^{\Delta/\Delta}$ MEFs—probably because the iron-sulfur cluster of IRP1 is readily destabilized by exposure to oxygen in cultured cells, leading to conversion of holo-IRP1 to the IRE-binding, apo-IRP1 form. Given the predominance of holo-IRP1 and the conversion of only a small fraction of this form to apo-IRP1 in mouse tissues (Meyron-Holtz et al., 2004a), the amount of apo-IRP1 in the liver of *Alb*-Cre/*Fbxl5*$^{F/F}$ mice may be masked by the more abundant holo-IRP1, which is not degraded by FBXL5 (Salahudeen et al., 2009; Vashisht et al., 2009). The upregulation of IRP2 in the liver of *Alb*-Cre/*Fbxl5*$^{F/F}$ mice was also associated with increased TfR1 expression (Figure 5O) and iron accumulation specifically in the liver (Figure 5P). The abundance of ferritin in the liver of *Alb*-Cre/*Fbxl5*$^{F/F}$ mice was paradoxically also increased despite the accumulation of IRP2 (Figure 5O). The amount of mRNA for the L chain of ferritin in the liver was greater for *Alb*-Cre/*Fbxl5*$^{F/F}$ mice than for *Fbxl5*$^{F/F}$ littermates, and this increase was greatly enhanced under conditions of oxidative stress induced by feeding the animals a high-iron diet (Figure S5C). Given that iron loss induces degradation of ferritin by the proteasome (De Domenico et al., 2006), both transcriptional and posttranslational mechanisms may contribute to upregulation of ferritin that dominates over IRP-mediated translational suppression of ferritin mRNA in the liver of *Alb*-Cre/*Fbxl5*$^{F/F}$ mice.

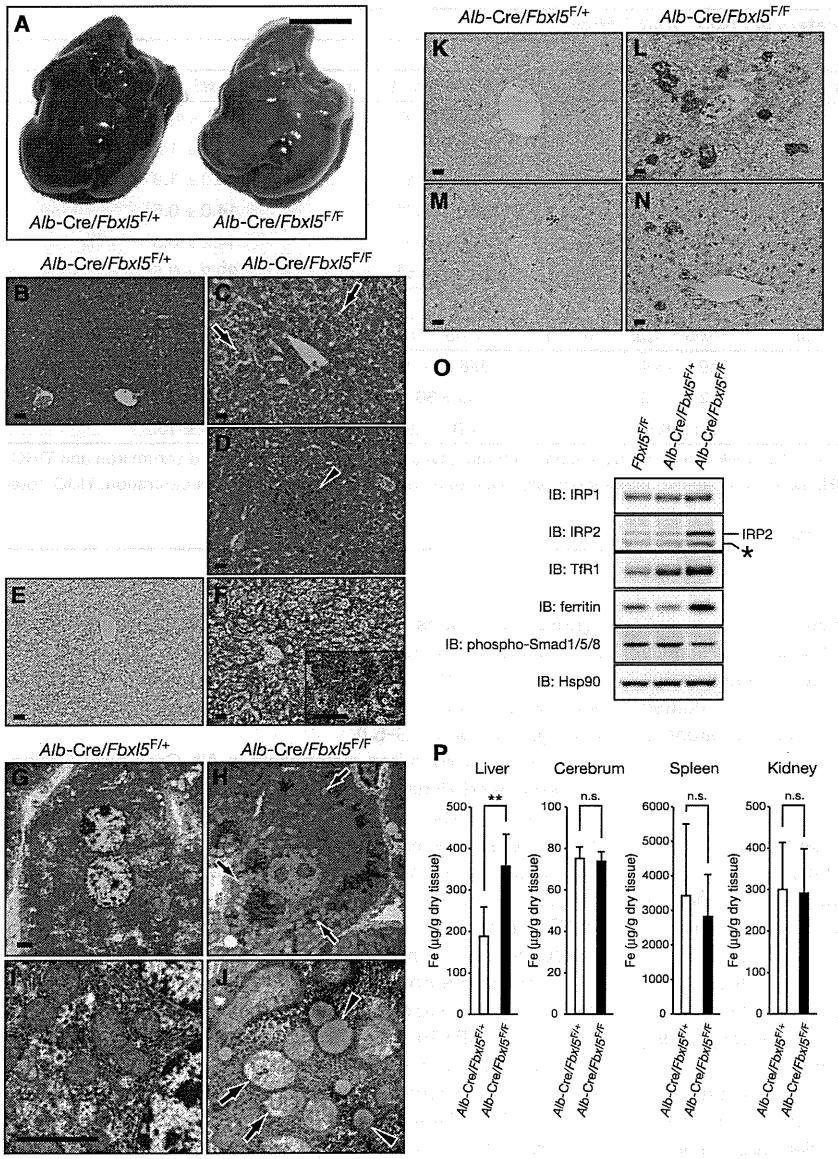

Figure 5. Hepatocyte-Specific Ablation of *Fbxl5* Results in Iron Accumulation and Steatohepatitis

(A) Gross appearance of the liver of *Alb*-Cre/*Fbxl5*$^{F/+}$ and *Alb*-Cre/*Fbxl5*$^{F/F}$ mouse littermates at 32 weeks of age. Scale bar, 10 mm.

(B–F) Histological analysis of the liver of 16- to 32-week-old *Alb*-Cre/*Fbxl5*$^{F/F}$ mice (C, D, and F) compared with that of control *Alb*-Cre/*Fbxl5*$^{F/+}$ littermates (B and E). (B–D) Hematoxylin and eosin staining. Arrows indicate numerous microvesicular vacuoles, and the arrowhead indicates lobular infiltration of inflammatory cells. (E and F) Oil red O staining. The inset in (F) shows a corresponding higher-magnification view. Asterisks indicate cell nuclei. Scale bars, 20 μm.

(G–J) Electron microscopy of the liver of 12-week-old *Alb*-Cre/*Fbxl5*$^{F/F}$ mice (H and J) compared with that of control *Alb*-Cre/*Fbxl5*$^{F/+}$ littermates (G and I). Arrows indicate numerous pale and swollen mitochondria, and the arrowheads indicate numerous lipid droplets. Scale bars, 2 μm.

(K–N) DAB-enhanced Perls staining (K and L) and DAB-enhanced Turnbull staining (M and N) of the liver of 16- to 32-week-old *Alb*-Cre/*Fbxl5*$^{F/F}$ mice (L and N) compared with that of control *Alb*-Cre/*Fbxl5*$^{F/+}$ littermates (K and M). Scale bars, 20 μm.

(O) Immunoblot analysis of liver extracts from 15-week-old mice of the indicated genotypes with antibodies to the indicated proteins. The asterisk indicates a nonspecific band.

(P) Nonheme iron content of the indicated organs of *Alb*-Cre/*Fbxl5*$^{F/+}$ (n = 4) and *Alb*-Cre/*Fbxl5*$^{F/F}$ (n = 8) mice at 16–32 weeks of age. Data are mean ± SD. n.s., not significant. **p < 0.01 (Student's t test). See also Figure S5 and Table S1.

Systemic Iron Overload in *Alb*-Cre/*Fbxl5*$^{F/F}$ Mice

We next asked how liver-specific deletion of *Fbxl5* affects systemic iron homeostasis. Serum iron levels (Figure 6A) as well as transferrin saturation (Figure 6B) were significantly increased in *Alb*-Cre/*Fbxl5*$^{F/F}$ mice, whereas hematologic parameters were not changed (Table S1). These results suggested that, inappropriately for their overall iron status, these mice might express low levels of hepcidin, the negative regulator of iron transport into plasma. The abundance of hepcidin mRNA in the liver was indeed significantly smaller for *Alb*-Cre/*Fbxl5*$^{F/F}$ mice than for *Fbxl5*$^{F/F}$ littermates (Figure 6C), and such a difference was also apparent when hepcidin gene expression was increased by feeding the animals a high-iron diet.

To elucidate the mechanism underlying the downregulation of hepcidin mRNA in the liver of *Alb*-Cre/*Fbxl5*$^{F/F}$ mice, we examined bone morphogenetic protein (BMP) signaling, which is the predominant regulator of hepcidin gene transcription (Hentze et al., 2010). Whereas the hepatic abundance of Hfe2 mRNA was unaffected (Figure S6A), that of BMP6 mRNA was smaller for *Alb*-Cre/*Fbxl5*$^{F/F}$ mice than for *Fbxl5*$^{F/F}$ littermates, and this difference was also apparent when *Bmp6* expression was increased by feeding the animals a high-iron diet (Figure S6B). We also examined receptor-activated Smad phosphorylation and found that the phosphorylation level of Smad1, Smad5, and Smad8 (Smad1/5/8) was decreased in the liver of *Alb*-Cre/*Fbxl5*$^{F/F}$ mice (Figure 5O). The amounts of mRNAs for suppressors of hepcidin gene transcription such as Smad6, Smad7, and transmembrane serine protease 6 (Tmprss6) were not increased in the liver of *Alb*-Cre/*Fbxl5*$^{F/F}$ mice, but rather were paradoxically decreased (Figure S6C). Increased iron did not activate Smad7 transcription in the liver of *Alb*-Cre/*Fbxl5*$^{F/F}$ mice, likely as a result of decreased BMP signaling (Kautz et al., 2008). Collectively, these findings indicated that BMP signaling in the liver of *Alb*-Cre/*Fbxl5*$^{F/F}$ mice is decreased as a result of the reduced expression of *Bmp6*, and they suggested that the decrease in *Bmp6* expression is likely responsible for downregulation of

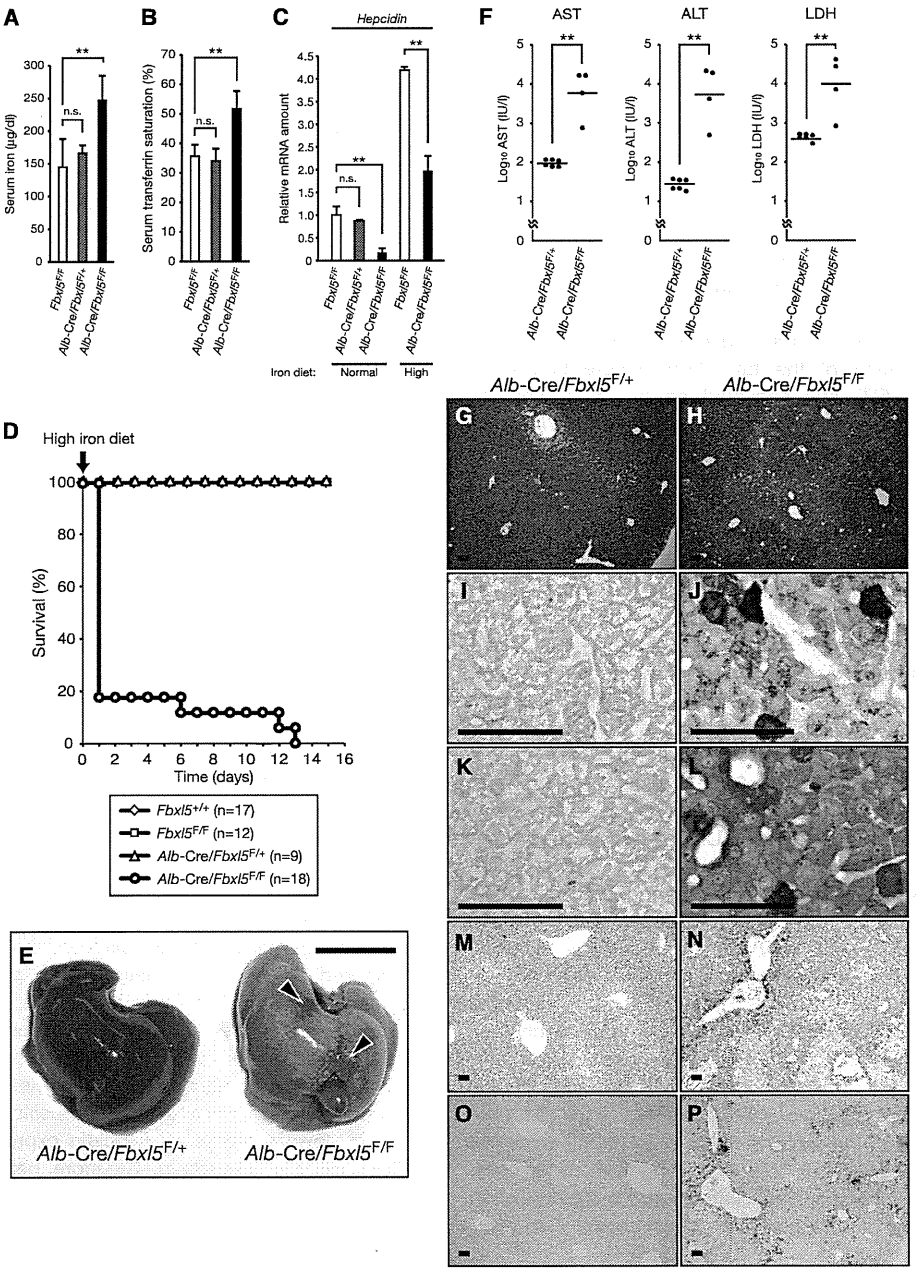

Figure 6. Fatal Liver Failure in *Alb*-Cre/*Fbxl5*$^{F/F}$ Mice Fed a High-Iron Diet

(A) Serum nonheme iron concentration in *Fbxl5*$^{F/F}$ (n = 4), *Alb*-Cre/*Fbxl5*$^{F/+}$ (n = 6), and *Alb*-Cre/*Fbxl5*$^{F/F}$ (n = 7) mice at 16–32 weeks of age. Data are mean ± SD. n.s., not significant. **p < 0.01 (Student's t test).

(B) Serum transferrin saturation in *Fbxl5*$^{F/F}$ (n = 3), *Alb*-Cre/*Fbxl5*$^{F/+}$ (n = 6), and *Alb*-Cre/*Fbxl5*$^{F/F}$ (n = 8) mice at 16–32 weeks of age. Transferrin saturation was calculated from measured total (TIBC) and unsaturated (UIBC) iron-binding capacities. Data are mean ± SD. **p < 0.01 (Student's t test).

(C) RT and real-time PCR analysis of hepcidin mRNA in the liver of 16-week-old mice of the indicated genotypes fed a normal diet or exposed to a high-iron diet for 1 day. Normalized data are expressed relative to the corresponding value for control mice (*Fbxl5*$^{F/F}$ mice fed a normal diet) and are mean ± SEM (n = 3 mice per group). **p < 0.01 (Student's t test).

(D) Kaplan-Meier survival curves for 6-week-old mice of the indicated genotypes after the start of a high-iron diet.

(E) Gross appearance of the liver of 6-week-old *Alb*-Cre/*Fbxl5*$^{F/+}$ and *Alb*-Cre/*Fbxl5*$^{F/F}$ littermates at 1 day after the start of a high-iron diet. Arrowheads indicate bleeding. Scale bar, 10 mm.

(F) Serum AST, ALT, and LDH activities in 6-week-old *Alb*-Cre/*Fbxl5*$^{F/+}$ (n = 6) and *Alb*-Cre/*Fbxl5*$^{F/F}$ (n = 4) mice at 1 day after the start of a high-iron diet. The results are plotted on a logarithmic ordinate, and horizontal lines indicate mean values. **p < 0.01 (Student's t test).

hepcidin in the liver of these mice. They further suggested that liver-specific ablation of FBXL5 results in systemic iron overload as a result of a reduced level of hepcidin secretion from the liver.

Fatal Liver Failure in *Alb*-Cre/*Fbxl5*$^{F/F}$ Mice Fed a High-Iron Diet

Given that hepcidin expression was downregulated in *Alb*-Cre/*Fbxl5*$^{F/F}$ mice, we next examined the effect of iron overload in these animals fed a high-iron diet. Whereas all control mice remained alive, most *Alb*-Cre/*Fbxl5*$^{F/F}$ mice died within 1 day, and the rest ate very little of the diet and lost weight, finally dying of starvation within 2 weeks (Figure 6D). Macroscopic examination of the *Alb*-Cre/*Fbxl5*$^{F/F}$ mice revealed prominent hemorrhage on the surface of the fatty liver (Figure 6E). Both prothrombin time (PT) and activated partial thromboplastin time (APTT) were significantly increased for *Alb*-Cre/*Fbxl5*$^{F/F}$ mice on the high-iron diet compared with those for *Fbxl5*$^{F/F}$ mice (Figure S6D), suggestive of a severe coagulopathy in the former animals. Serum levels of hepatic enzymes such as aspartate aminotransferase (AST), alanine aminotransferase (ALT), and lactate dehydrogenase (LDH) were also increased ~100-fold in these animals (Figure 6F), suggestive of an acute progressive destruction of hepatocytes. Changes in biliary tract enzymes were smaller than those in hepatic enzymes (Table S2). Histological analysis revealed massive cell death, predominantly in the area around portal veins, in the FBXL5-deficient liver (Figures 6G and 6H). DAB-enhanced Perls or Turnbull staining also revealed the accumulation of ferrous iron in the hepatocytes of *Alb*-Cre/*Fbxl5*$^{F/F}$ mice (Figures 6I–6L), whereas detection of 4-HNE-modified proteins revealed a marked increase in oxidative stress (Figures 6M and 6N). TUNEL-positive cells were also observed among hepatocytes of *Alb*-Cre/*Fbxl5*$^{F/F}$ mice (Figures 6O and 6P). Furthermore, oxidative stress and cell death in the liver were markedly attenuated by the addition of NAC to the drinking water of *Alb*-Cre/*Fbxl5*$^{F/F}$ mice fed the high-iron diet (Figure S6E). On the other hand, *Irp2*$^{-/-}$ mice did not die when fed a high-iron diet (n = 6, data not shown), probably because the accumulation of ferrous iron was much less pronounced than was that of ferric iron in these animals (Figure S6F). Given that the high-iron diet had little effect on the iron content of other organs of *Alb*-Cre/*Fbxl5*$^{F/F}$ mice (data not shown), these results indicated that *Alb*-Cre/*Fbxl5*$^{F/F}$ mice fed such a diet died of acute liver failure resulting from iron excess. Collectively, our observations implicate FBXL5 in the regulation of iron homeostasis both at the systemic level and in the liver.

DISCUSSION

We have shown that the loss of FBXL5 results in upregulation of IRP expression and activity, leading to fatal damage in embryos or the adult liver due to the excessive accumulation of ferrous iron. Our genetic evidence suggests that IRP2 is the major target of the SCF^{FBXL5} E3 ligase. Our findings further indicate that FBXL5 plays a central role in the maintenance of appropriate concentrations of intracellular iron and is essential for embryonic development as well as for normal postnatal liver physiology in mice.

Regulation of IRP activity is essential for cells to maintain an appropriate cytosolic LIP, thereby avoiding deleterious iron deficiency and preventing iron excess. FBXL5 recognizes both IRP1 and IRP2 and promotes their degradation in an iron-dependent manner. Our results now indicate that iron-dependent degradation of IRPs mediated by FBXL5 is pivotal for regulation of their activity as well as for iron homeostasis in mice. FBXL5 also senses intracellular iron through direct iron binding to its hemerythrin domain, resulting in FBXL5 stabilization (Salahudeen et al., 2009; Vashisht et al., 2009). Thus, FBXL5 acts as a sensor of the cytosolic LIP that negatively regulates this pool through degradation of IRPs.

Maintenance of the cytosolic LIP at an appropriate level is crucial, especially in cells exposed to iron overload. We found that *Fbxl5*$^{-/-}$ embryos die manifesting iron accumulation in the early placenta, and that *Fbxl5*$^{-/-}$ blastocysts do not survive under iron-replete conditions. These results suggest that FBXL5 is a key regulator that confers resistance to stress resulting from iron overload. During embryogenesis, FBXL5 plays an essential role in the early placental regions. Given that mice lacking the iron-exporting protein ferroportin, which transfers iron from the extraembryonic visceral endoderm (early placenta) into the embryo, die in utero (Donovan et al., 2005), these early placental regions appear to be essential for iron delivery to embryos, and they thereby need to endure stress attributable to iron overload. FBXL5 appears to protect these iron-transferring cells from damage due to excess iron.

FBXL5 also plays an essential role in normal postnatal liver physiology by preventing systemic iron overload. Hereditary hemochromatosis is a genetic disorder that leads to iron overload in the liver and other organs. Complications of this disease include liver cirrhosis, cancer, diabetes, and heart failure. To date, hereditary hemochromatosis has been attributed to defects in five genes, four of which give rise to recessive disorders (De Domenico et al., 2008). All recessive forms of the disease are associated with molecular defects in hepatocytes and are caused by inappropriately low levels of hepcidin expression. We have now shown that liver-specific ablation of FBXL5 results in downregulation of hepcidin expression and consequent systemic iron overload. Therefore, hepatic expression of FBXL5 might also be a determinant of iron overload disorders.

Iron overload status in FBXL5-deficient mice differs substantially from that in other mice showing simple systemic iron overload in terms of the valence of the accumulating iron (Fe^{2+} or Fe^{3+}). FBXL5-deficient mice manifest accumulation of dangerous ferrous iron (Fe^{2+}), whereas many other animal models such as mice deficient in Hfe1 (Zhou et al., 1998), Hfe2 (Niederkofler et al., 2005), or hepcidin (Lesbordes-Brion et al., 2006) exhibit accumulation of ferric iron (Fe^{3+}) in the liver as a result of defective hepcidin production. This point is key to understanding iron metabolism in *Alb*-Cre/*Fbxl5*$^{F/F}$ mice, which

(G–P) Histological analysis of the liver of 6-week-old *Alb*-Cre/*Fbxl5*$^{F/F}$ mice (H, J, L, N, and P) and control *Alb*-Cre/*Fbxl5*$^{F/+}$ littermates (G, I, K, M, and O) at 1 day after the start of a high-iron diet. Hematoxylin and eosin staining is shown in (G) and (H), DAB-enhanced Perls staining is shown in (I) and (J), DAB-enhanced Turnbull staining is shown in (K) and (L), immunohistochemical staining with antibodies to 4-HNE is shown in (M) and (N), and TUNEL staining is shown in (O) and (P). Scale bars, 100 μm. See also Figure S6 and Table S2.